Experiments in Fluids (2026) 67:33
https://doi.org/10.1007/s00348-026-04184-4

RESEARCH ARTICLE

Aerodynamic excitations in the near wake of space launchers: insights from hot-flow experiments using high-speed PIV

Dominik Saile[1] · Viktor Kühl[1] · Ali Gülhan[1]

Received: 10 September 2025 / Revised: 23 December 2025 / Accepted: 26 January 2026

Abstract

The catastrophic failure of the Ariane 5 ECA heavy launcher in December 2002 underscored significant gaps in understanding the dynamic loads acting on the vehicle's base region. Investigations revealed that aerodynamic interactions between the nozzle exhaust plume and the launcher wake, particularly the phenomenon of "buffeting," led to intense oscillatory mechanical loads. This study addresses the challenges in accurately replicating these effects in both experimental and numerical models, given the wide range of time and spatial scales and the complexities of high-temperature gas flows. Traditional experimental approaches have relied on cold nozzle flows, which, while practical, fail to capture key high-temperature effects influencing aerodynamic excitations. To overcome these limitations, a novel experimental setup was developed using a wind tunnel model integrated with a solid propellant combustion chamber, producing hot exhaust gases under realistic conditions. Advanced diagnostics, including high-speed particle image velocimetry (PIV) at 8500 Hz, high-speed schlieren imaging, and Kulite pressure sensors at 17000 Hz, enabled detailed characterization of the unsteady flow dynamics in the base region. Key findings reveal two dominant aerodynamic modes in the base region: flapping, characterized by asymmetric flow motion, and swinging, associated with symmetric oscillations. These modes are the primary drivers of the unsteady loads acting on the nozzle and adjacent structures. At a Mach number of 0.8, the flapping mode is found to resonate with the jet noise mechanism known as screeching, resulting in strong, alternating oscillatory loads on the wake region. This resonance amplifies the mechanical stresses experienced by the structure and, from the authors' perspective, represents the most plausible explanation for the excessive loads that led to the catastrophic failure of Ariane 5 Flight 157. The study successfully replicates realistic flight conditions for investigating buffeting phenomena, bridging the gap between cold-flow experiments and actual high-temperature exhaust flows. This achievement enhances predictive modeling capabilities by providing a more accurate understanding of the dynamic interactions in the base region. To support this, a schematic model of the feedback cycle was developed to visualize and capture the interacting effects, thereby facilitating a deeper physical understanding. Consequently, the research contributes to the development of safer and more efficient space launch systems by enabling improved design strategies to mitigate such damaging aerodynamic loads. The consistency of these results with prior cold-flow studies further validates the robustness of the experimental approach and the universality of the identified aerodynamic mechanisms across varying flow conditions.

1 Introduction

In the aftermath of the Ariane 5 failure, numerous research groups focused their efforts on characterizing and identifying the underlying mechanisms that led to the incident. This work was carried out within research initiatives such as Future European Space Transportation Investigation Programme (FESTIP) (1993) and the DFG-TRR40 (2020), yielding valuable insights into the aerodynamics of the Ariane 5 across a wide flight regime—from subsonic to hypersonic speeds—using both numerical and experimental approaches. To manage the complexity and isolate specific effects, the geometry of the Ariane 5 was simplified using generic volume elements. Thanks to the breadth of results and the abstracted geometric representation, which enabled the identification of common scientific patterns, this test case effectively became a benchmark within the research community.

✉ Dominik Saile
Dominik.Saile@DLR.de

[1] DLR Institute of Aerodynamics and Flow Technology, Supersonic and Hypersonic Technologies Department, Linder Höhe, 51147 Koln, Germany

Published online: 14 February 2026

The time-averaged flow behavior around a simplified base model exposed to high-subsonic ambient conditions is depicted in Fig. 1. The schematic, adapted from Saile (2019a), presents a scenario involving an over-expanded, supersonic exhaust jet. As the freestream encounters the abrupt contour at the model's shoulder, it detaches—evolving into a free shear layer eventually intersecting with the jet under the given conditions. Between the jet, the base surface, the nozzle wall, and the shear layer, a large recirculation region is enclosed that, when viewed in time-averaged terms, is dominated by a large vortex. Depending on the configuration, the shear layer reattaches either solely on the jet (as shown in Fig. 1), solely on the solid nozzle wall, or alternates between the two. The latter behavior is referred to in the literature Gent et al. (2019) as hybrid reattachment.

The time-averaged flow field alone does not explain the excessive loads that led to the failure. Instead, it is an unsteady flow phenomenon—specifically the interaction between the wake flow and downstream structures, such as the nozzle—that plays a crucial role. This phenomenon is known as buffeting. Real flight data documented in David and Radulovic (2005) have shown that the strongest loads occur in the subsonic regime, particularly around Mach 0.8. For this reason, the subsonic flow conditions have become the focus of many investigations, including the present study. Numerous numerical Deck and Thorigny (2007); Weiss et al. (2009); Weiss and Deck (2013); Statnikov (2016); Statnikov et al. (2017); Pain and Weiss (2014); Pain et al. (2019) and experimental Depr et al. (2004); Wolf (2014); Schrijer et al. (2014); Roquefort et al. (2005); Schrijer et al. (2011); Gentile et al. (2016a, 2016b); Gent et al. (2018); Gent et al. (2019); Saile et al. (2019b, 2019c); Saile et al. (2021); Kirchheck et al. (2019) studies have found that the wake flow in this regime is dominated by a phenomenon known as shear layer cross-flapping. This motion is characterized by antisymmetric oscillations of the mutually interacting shear layers in the wake. The term "cross" refers to a wave-like pattern in the azimuthal direction or, in a 2D representation, the spanwise direction (Statnikov 2016). These oscillations typically occur at a Strouhal number $\mathrm{Sr_D}$ in the range of 0.18 to 0.2, where the Strouhal number is defined as $\mathrm{Sr_D} = fD/U_\infty$, with f being the frequency measured in the wake, D the base diameter, and U_∞ the free-stream velocity. These primary oscillations are often accompanied by modes at half and double the dominant frequency (see, e.g., Statnikov et al. (2017); Saile (2019a)). The lower-frequency mode corresponds to a symmetric "pumping" motion, associated with the growth and decay of the recirculation bubble. The higher-frequency mode involves a smaller-scale swinging of the shear layer at approximately half the characteristic length scale.

The unsteady wake flow phenomena discussed above still do not fully explain why oscillations are strongly amplified in the high-subsonic flow regime, especially since such oscillations occur across all Mach numbers. This specific aspect was addressed in Saile (2019a); Saile and Gülhan (2021), where strong amplification effects were observed in experiments involving a cold exhaust jet. The amplification was attributed to a resonant feedback mechanism between wake flow instabilities and jet noise generated by the screeching phenomenon. As described in Powell (1953a, 1953b), the screeching mechanism operates as follows: An embryonic disturbance originates at the nozzle lip, grows as it propagates downstream, interacts with the shock cells

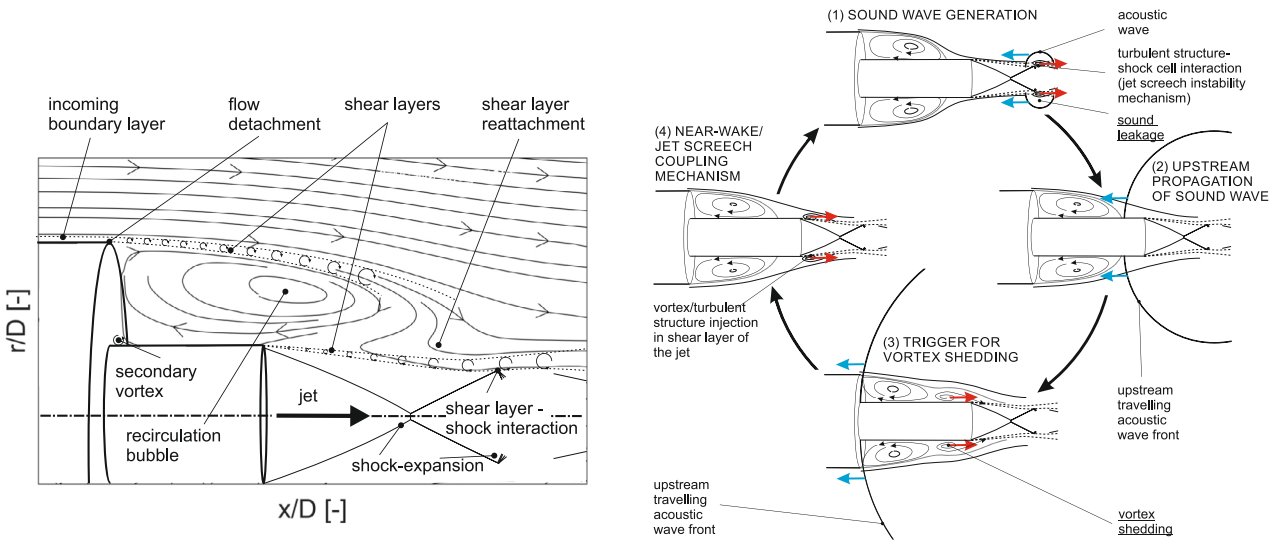

Fig. 1 Left: Mean base flow topology and flow features in the subsonic wake of space launcher configuration with jet. Right: Aeroacoustic coupling between jet screech and the near-wake dynamics. Both graphs are reproduced from Saile (2019a); Saile and Gülhan (2021)

to produce sound, and finally the sound generated propagates upstream to the nozzle lip, thus closing the resonant loop. In-flight screeching has been documented for aircraft, typically at lower Mach numbers, where it can lead to material fatigue near the engine exhaust (Hay and Rose 1970; Bryce and Pinker 1977; André 2011). In rocket base flows, screeching has also been identified in the pressure spectrum at low Mach numbers (Wolf 2014). For in-flight scenarios, the characteristic screech frequency can be calculated using the following relation (Wolf (2014); Saile (2019a)):

$$f_s = \frac{U_{\text{conv}}}{L_{\text{cell}}\left(1 + \frac{U_{\text{conv}}}{a_\infty - U_\infty}\right)}, \tag{1}$$

where L_{cell} is the length of a shock cell in the jet's shock train, and a_∞, U_∞, and U_{conv} denote the speed of sound in the free-stream, the free-stream velocity, and the convective velocity of a disturbance in the shear layer, respectively. The convective velocity is given by:

$$U_{\text{conv}} = 0.7 \cdot (U_j - U_\infty) + U_\infty, \tag{2}$$

with U_j representing the jet velocity.

The novelty presented in Saile (2019a); Saile and Gülhan (2021) lies in establishing a direct link between screeching and near-wake flow instabilities. In contrast to the classical mechanism described in Powell (1953a, 1953b), the disturbances that feed into the jet's shear layer originate from the base shear layer and the vortices shed due to its motion. Furthermore, it was shown that the frequency of near-wake flow excitations increases with rising Mach numbers, whereas the screeching frequency decreases due to the increasing ambient flow velocity. This opposing trend inevitably leads to resonance at high-subsonic Mach numbers for the given configuration. The resulting resonance, in turn, causes a significant amplification of pressure fluctuations in the base region—a phenomenon that can become hazardous in real flight conditions. In the experiments, the use of a cold-flow jet with smaller shock cells—chosen to avoid condensation in the exhaust by limiting chamber pressure—led to resonance occurring at Mach 0.8 for the near-wake flow instability mode known as "swinging." The corresponding feedback loop mechanism is illustrated in Fig. 1.

In comparison to real flight conditions, it remains to be demonstrated whether the excitation mechanisms described above also apply when hot exhaust jets are present. Internal discussions initially led to the hypothesis that the thinner shear layers characteristic of hot jets might be less receptive to disturbances, making them less prone to grow as they are convected downstream. Such a behavior would imply a delayed jet decay, reduced shock leakage of acoustic pressure waves, and consequently a weakening of the closed-loop resonance mechanism.

However, this interpretation alone would not explain the excessive dynamic loads observed during the Ariane 5 ECA failure. In real flight, the asymmetric flapping motion is known to be dominant, and due to the alternating excitation of structures in the base region, this mode is significantly more hazardous than the symmetric swinging mode observed in cold jet experiments (Saile 2019a; Saile and Gülhan 2021). We therefore advance an alternative hypothesis: Under flight-relevant hot-flow conditions, the base region shear layer remains susceptible to asymmetric flapping and can enter resonance with jet screech in the transonic regime. Such a resonance would amplify alternating pressure loads and provide a physically consistent explanation for the damage observed in flight.

Although previous studies have pointed to the potential for asymmetric excitation, it has not yet been demonstrated whether this excitation can occur in resonance with the flapping mode under hot jet conditions. Addressing this open question is a central objective of the present study, which investigates a hot exhaust jet released from a high-pressure, high-temperature combustion chamber ($p_{CC} \sim 60$, bar and $T_{CC} \sim 2560$, K), representing conditions comparable to those encountered in real flight.

2 Methods

This section introduces the VMK wind tunnel and the experimental setup, including the wind tunnel model, the measurement techniques—such as particle image velocimetry, high-speed schlieren imaging, and pressure sensing—and provides a general overview of the data analysis approach.

The Vertical Test Section (VMK) in Cologne is a wind tunnel specifically designed to replicate the aerothermodynamic loads experienced by high-speed flight vehicles operating at Mach numbers between 0.5 and 3.2. It enables the simulation of sea-level conditions even at high Mach speeds. Over the years, VMK has been used extensively to investigate re-entry capsules, ramjets, scramjets, missiles, and space launch systems.

This blow-down-type wind tunnel is distinguished by three key features: (1) The airflow exits the nozzle vertically, (2) the test section is open, and (3) the measurement chamber is enclosed within a reinforced, overpressure-protected concrete tower. These characteristics make VMK particularly well-suited for free-flight testing of aerodynamic models and the integration of advanced, complex measurement techniques. Its open design offers direct optical access and generous space, facilitating detailed diagnostics. Moreover, the facility is capable of accommodating propulsion systems, including those involving explosive components—capabilities that were both utilized in the present study.

The tests conducted for this investigation were performed in the subsonic Mach number range of 0.6 to 0.9, achieved by adjusting the reservoir pressure. The airflow was unheated. Owing to the open test section design, the free-stream pressure naturally equaled the ambient atmospheric pressure.

The test setup is illustrated in Fig. 2. The left image presents a cross-sectional view of the test specimen, which comprises a wind tunnel model integrated into a subsonic wind tunnel nozzle. The model is centrally mounted near the nozzle inlet using two vertically aligned struts positioned at 90-degree intervals around the nozzle circumference. These struts serve as conduits for routing the pressure sensor wiring to the data acquisition system. A similar configuration has been employed in several previous measurement campaigns, demonstrating its reliability and effectiveness for such experimental investigations (Saile 2019a; Saile and Gülhan 2021; Saile et al. 2013; Kirchheck et al. 2019; Kirchheck et al. 2019, 2021).

Part of the wind tunnel model includes the integrated rocket motor, located in the upper section of the model. The motor operates using two PRO 54 solid propellant grains manufactured by Cesaroni Technology. These are BATES-type grains, each with a length of 84 mm, an inner diameter of 16 mm, and an outer diameter of 47.5 mm. The grains consist of a composite propellant based on ammonium perchlorate (AP), hydroxyl-terminated polybutadiene (HTPB), and aluminum (4.5 % Al). Ignition is achieved using a pyrotechnic initiator.

The nozzle has a throat diameter of 8.2 mm. In combination with the selected solid propellant grains, this results in a measured maximum combustion chamber pressure of approximately 6 MPa. Using the Rocket Propulsion Analysis (RPA) tool Ponomarenko (2014), the corresponding combustion chamber conditions are estimated as follows: A temperature of 2560 K, an isentropic exponent of $\kappa = 1.21$, and a specific gas constant of $R_s = 348.8\,\mathrm{J/(kg \cdot K)}$. The nozzle exit diameter is 25.8 mm, giving an expansion ratio of $\epsilon = 9.9$. This corresponds to an exit Mach number of 3.4, an exit velocity of 2368 m/s, and an exit pressure of 0.642 bar, based on a one-dimensional approximation. These values indicate that the nozzle operates in an over-expanded regime. However, no evidence of flow separation was observed during testing. Additionally, according to the criteria presented in Stark and Wagner (2009), flow separation within the nozzle is not expected under these conditions. The conical nozzle has a total opening angle of 15° (7.5° half-angle). The nozzle lip thickness is 0.5 mm, and the throat region is protected by a graphite liner to withstand the high thermal loads.

A conical nozzle was chosen instead of the thrust-optimized parabolic (TOP) nozzle used in the Vulcain 2 rocket engine. This choice was motivated by several considerations. First, the conical nozzle follows a simple geometric definition, making it straightforward to reproduce and manufacture, either in-house or by other research groups for verification and comparison studies, or to replace when it is damaged or destroyed due to high thermal loads. Second, it allows for easy adjustment of the expansion ratio. This flexibility was essential for the preceding cold-flow experiments (Saile 2019a) to mitigate condensation effects and control nozzle flow separation. Moreover, for hot-gas experiments using solid propellants (not discussed here but conducted separately), increasing the

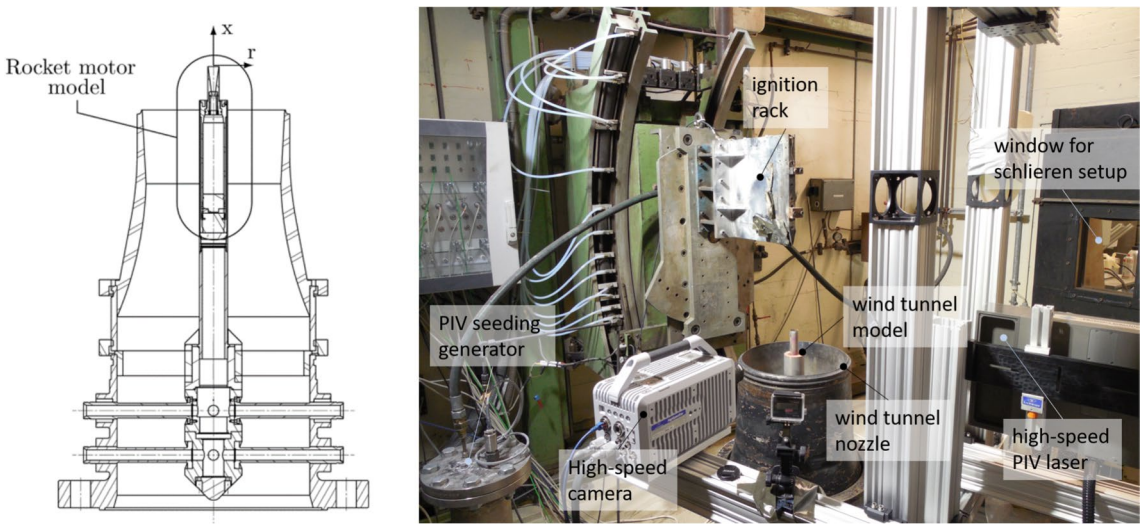

Fig. 2 A schematic illustration (left) depicts the wind tunnel model integrated into the wind tunnel nozzle, including details of the solid rocket motor; the picture (right) shows the VMK wind tunnel environment with the test model, PIV system, and high-speed schlieren measurement setup

throat diameter provides a convenient means of varying the combustion chamber pressure for a given propellant grain configuration. Third, the flow within a conical nozzle does not exhibit nozzle-specific recompression shocks, which are typically present in optimized nozzle designs. Fourth, the exit flow conditions are relatively uniform in the radial direction (see Figs. 4.5 and 4.6), simplifying interpretation of the downstream flow behavior. Finally, the primary focus of the present work is on understanding the underlying physical mechanisms rather than achieving an exact duplication of the Ariane 5 internal flow field. In summary, although the internal nozzle geometry differs from that of Ariane 5, this deviation was deliberately accepted based on the methodological and practical advantages outlined above.

The outer shape of the model generically replicates the base geometry of Ariane 5. The ratio between the diameter D of the outer shell and the nozzle diameter d is 0.4, while the nozzle length L is 1.2 times the outer shell diameter, which measures 67 mm. The identical model was previously employed in Saile et al. (2013). An image of the wind tunnel model integrated into the VMK facility, along with the setup for several measurement techniques, is shown on the right side of Fig. 2. Positioned above the nozzle is the ignition rack, which was used to guide the igniter through the nozzle for initiating combustion.

The measurement techniques: High-speed particle image velocimetry (PIV), high-speed schlieren imaging, and pressure measurements—both in the combustion chamber and at the base of the rocket model—were employed in this study. The placement of the PIV components is also shown in Fig. 2. The PIV was performed in a 2D-2C configuration, with the high-speed camera positioned perpendicular to the laser sheet. The system consists of a Photron SA-X / HighSpeedStar X high-speed camera and a dual-cavity Nd:YLF laser (DM30-527-DH) from Photonics Industries. The laser operates at a wavelength of 527 nm and is capable of delivering 30 mJ per pulse at a repetition rate of 1 kHz. For the present study, laser cavities 1 and 2 were set to powers of 28 W and 26 W, respectively, at a repetition rate of 8500 Hz. The laser beam was shaped using light sheet optics with a focal length of $f = -20$ mm. The camera was equipped with a 50 mm focal length lens, resulting in a field of view of approximately $130 \times 130\,\mathrm{mm}^2$ (7.83 px/mm), with the aperture set to f/5.6. The working distance for both the camera and laser was about 45 cm. Synchronization of the components was achieved using a LaVision High-Speed Controller (HSC). Titanium dioxide particles from Kronos International Inc. were used as the seeding material. These particles have a number-based median diameter of $d_{50n} = 0.2\,\mu$m. Seeding was introduced upstream of the subsonic wind tunnel nozzle using an in-house developed generator. The PIV evaluation was performed using a multi-pass approach with four passes. The final interrogation window size was 32×32 pixels, with a 75% overlap between adjacent windows.

The window designated for the schlieren setup indicates the optical path used for schlieren imaging. A Z-type schlieren configuration was employed for this purpose. Recordings were acquired using a Photron Fastcam APX-RS camera operating at a frame rate of 17 kHz. The field of view, approximately $121 \times 116\,\mathrm{mm}^2$, was captured with a resolution of 384×368 px.

Nine flush-mounted, piezo-resistive pressure transducers of type XCQ-080-0.35BARSG from Kulite are integrated into the base to measure the base pressure and its fluctuations. Seven of these sensors are arranged azimuthally at a radial position of $r/R = 0.74$ (with $R = 67/2$ mm), corresponding to relative angular positions of 0°, 60°, 120°, 150°, 170°, 180°, and 190°. Additionally, two more sensors are positioned radially at an angle of 180°, located at $r/R = 0.64$ and $r/R = 0.83$. The reference pressure is set to 0.8 bar. The sensors are selected for a measurement range of 0.35 bar and have a typical combined error—accounting for nonlinearity, hysteresis, and repeatability—of ±0.1% of the best-fit straight line (BFSL) over the full-scale output. To monitor the combustion chamber pressure, a Kulite XTEL-24-140-70BAR sensor is used, which features the same BFSL accuracy specification. For redundancy, a Druck PDCR 135 pressure transducer is also installed, offering a higher accuracy of ±0.05% BFSL.

3 Results and discussion

The results concerning the spatio-temporal characteristics of the near-wake region are presented in the order of the flow direction. First, the pressure measurements taken from the base plate are discussed, followed by the PIV results in the base region. Finally, high-speed schlieren images of the jet are presented. The section concludes with the development of a schematic model that integrates these findings to explain the base flow dynamics.

Chapter "Appendix—Chamber Pressure & Mach disk" presents additional characteristics of the rocket motor, including the temporal evolution of chamber pressure and the pressure-dependent movement of the Mach disk within the jet (Fig. 19-1/2). While this information is valuable for numerical reconstruction of the experiment—also as a test case for ballistic modeling—it falls outside the main scope of the present study and is therefore provided in appendix.

The pressure fluctuations on the base are measured using flush-mounted pressure transducers integrated into the face plate. Figure 3 shows the evolution of the standard deviation of the pressure signal, as well as the corresponding pressure coefficient, throughout the combustion phase of the solid propellant and into the post-combustion period. The data

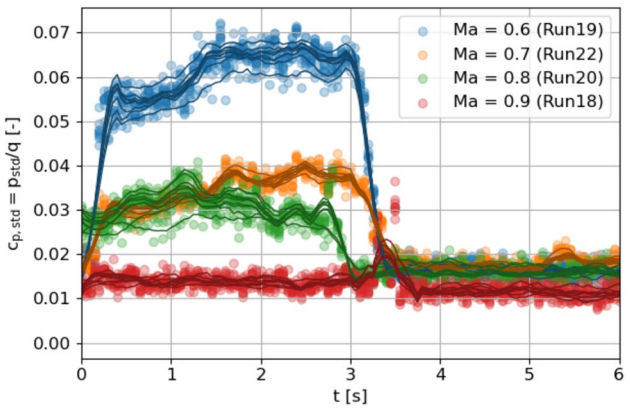

Fig. 3 Standard deviation evolution of the base pressure for the various Mach number cases. The standard deviation is generated over 850 samples, which are captured within 50 ms. The lines correspond to individual pressure sensors, while the data are smoothed by applying a Savitzky–Golay filtering

are shown for all investigated Mach numbers, namely Mach 0.6, 0.7, 0.8, and 0.9. Each data point in the plot represents a moving window of 850 samples to ensure statistical relevance. The individual curves correspond to the readings from the respective pressure sensors embedded in the face plate. This representation allows for a comparative analysis of how base pressure fluctuations evolve over time across different flow regimes and sensor locations.

The graph shows that the pressure fluctuation coefficient is—except for the Mach 0.9-case—significantly higher when the solid propellant motor is active. Specifically, the pressure fluctuations are amplified by a factor of approximately 1.5 to 3 when comparing the motor-on and motor-off conditions. Furthermore, a correlation appears between the fluctuation level and the combustion chamber pressure evolution (see Fig. 19-1). This correlation is most likely linked to the displacement effect of the expanding jet plume, which alters the base flow dynamics. However, it cannot be ruled out that other influences—such as combustion chamber pressure oscillations transmitted downstream to the base region—also contribute. The most pronounced amplification in relative terms is observed for Mach 0.6. In absolute terms, however, the Mach 0.8-case reaches similar levels of pressure fluctuation (not shown). For Mach 0.9, in contrast, the difference between the motor-on and motor-off conditions is minor. The presence of the jet increases fluctuations by only about 10%, a relatively small amplification compared to the lower Mach numbers. Previous studies (Saile 2019a; Saile and Gülhan 2021; Saile et al. 2019c) have shown that at Mach 0.9, the shear layer does not exhibit solid reattachment on the nozzle. Instead, a fluid reattachment occurs on the jet itself, which fundamentally alters the base flow dynamics. The current PIV results confirm that the same flow topology is present in the configuration studied here. Moreover, the measured pressure fluctuation coefficient $c_{p,\,\mathrm{std}}$ aligns well with the findings in Saile (2019a), considering the differences in setup. In the earlier work, cold jets at a chamber pressure of 2 MPa were used, whereas the current study involves a hot jet at 6 MPa. Reported values for $c_{p,\,\mathrm{std}}$ in Saile (2019a) were approximately 0.04, 0.03, and 0.01 for Mach numbers 0.6, 0.7, and 0.9, respectively. Further information is available in the referenced literature. The key takeaway from Fig. 3 is that the presence of an operating jet generally leads to an amplification of pressure fluctuations in the base region.

Naturally, it is of interest to identify the driving mechanisms behind the observed amplification of pressure fluctuations. Characteristic aspects of the spatio-temporal behavior can be examined through spectral analysis, which is presented in Fig. 4 as a spectrogram for one sensor located at $r/R = 0.74$ (results from the other sensors are qualitatively similar) across all tested Mach numbers. The spectrogram reveals pressure fluctuations that appear to correlate with the evolution of the combustion chamber pressure—particularly at Mach 0.6 and Mach 0.7, where the fluctuations increase in step with the rising chamber pressure (Fig. 19-1)—and are concentrated within distinct, relatively broad frequency bands. For Mach 0.6, pronounced excitations are observed in the frequency ranges of $f \lessapprox 260$ Hz, $590\,\mathrm{Hz} \lessapprox f \lessapprox 900\,\mathrm{Hz}$, $1300\,\mathrm{Hz} \lessapprox f \lessapprox 2200\,\mathrm{Hz}$, and $2600\,\mathrm{Hz} \lessapprox f \lessapprox 2800\,\mathrm{Hz}$. In the Mach 0.7-case, the excited frequency bands are generally shifted to lower values, with dominant ranges at $f \lessapprox 260\,\mathrm{Hz}$, $450\,\mathrm{Hz} \lessapprox f \lessapprox 830\,\mathrm{Hz}$, $1050\,\mathrm{Hz} \lessapprox f \lessapprox 1400\,\mathrm{Hz}$, and $1700\,\mathrm{Hz} \lessapprox f \lessapprox 1900\,\mathrm{Hz}$. The Mach 0.8-case is notable for its distinct spectral character, showing a dominant and narrow excitation peak centered around 700 Hz. In contrast, the Mach 0.9-case exhibits negligible excitation across the frequency spectrum, indicating a significantly different base flow behavior under these conditions.

In the following, the analysis focuses on the Mach 0.8-case. This scenario is chosen because it exhibits the most pronounced excitation, making it a promising candidate for identifying a dominant governing mechanism. Moreover, it holds particular relevance for real flight applications, as the distinct excitation poses a potential risk of resonance with structural components. Aerodynamic excitation becomes especially critical when it coincides with the natural frequency of the structure. For the configuration considered, Strouhal similarity yields a scaling factor of 80 between the wind tunnel model and an Ariane 5-like full-scale system ($D_{\mathrm{real}}/D_{\mathrm{model}} = 80$), corresponding to a frequency of approximately 9 Hz. This implies that large structures with eigenfrequencies in this range are particularly susceptible to such aerodynamic excitations and therefore at risk. Finally, previous studies based on actual flight data (David and Radulovic 2005) have shown that this Mach number regime is indeed the most critical along the trajectory of Ariane 5. Specifically, it was demonstrated that pressure fluctuations at the

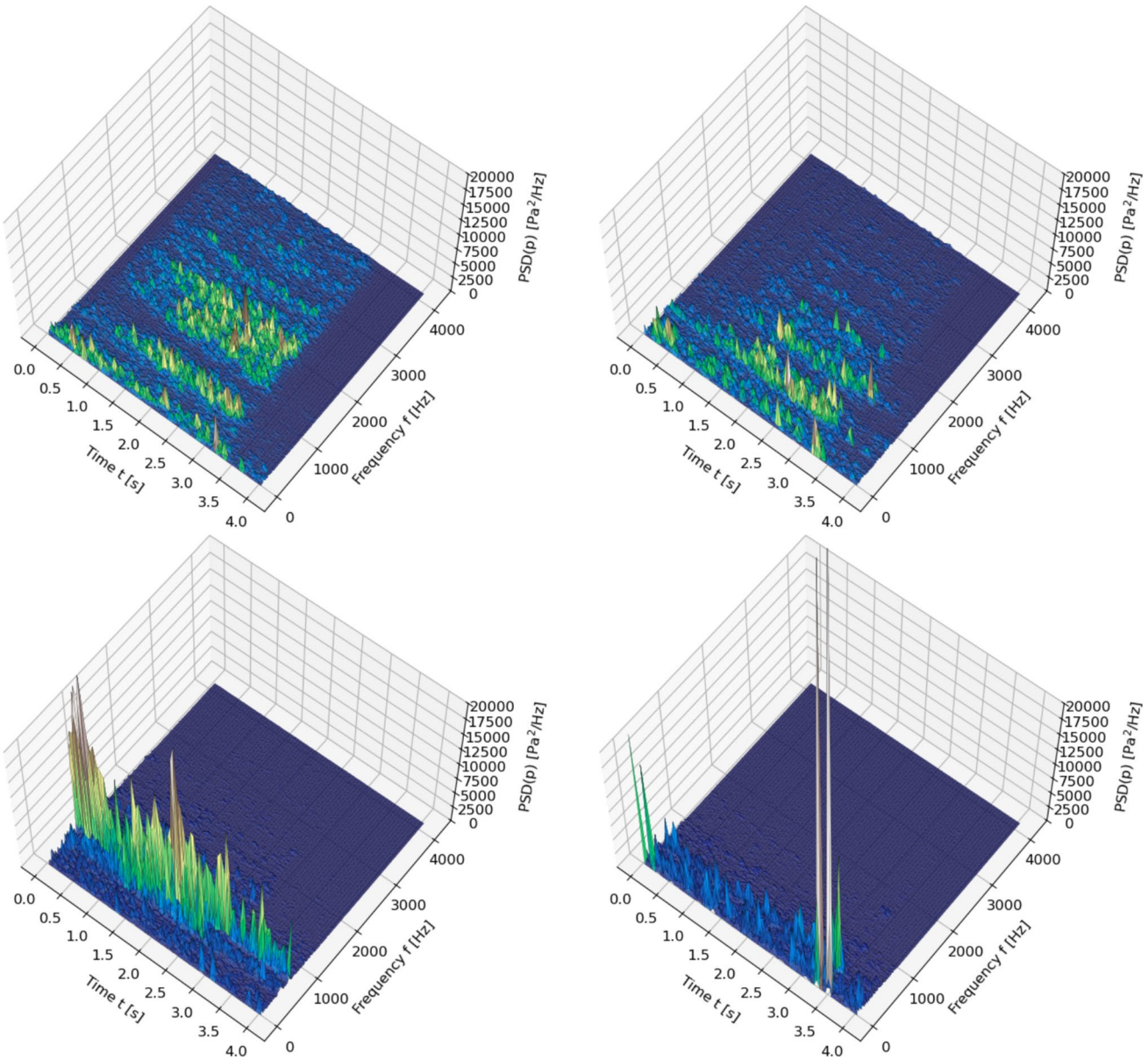

Fig. 4 Spectrograms of the base pressure fluctuations at Mach 0.6 (top left), 0.7 (top right), 0.8 (bottom left), and 0.9 (bottom right). Number per segment and number for fast Fourier transform are 1024, while applying a Tukey window with shape parameter of 0.25

base correlate with the activity of the actuator controlling the gimbaling system of the nozzle, further highlighting the importance of this flight phase in terms of buffeting risk.

Consequently, a close-up of the pressure spectrogram for the Mach 0.8-case is provided in Fig. 5. In addition, Fig. 6 illustrates the interdependence of the pressure signals recorded by the transducers on the base face plate for the dominant oscillation at 700 Hz. The first graph highlights a narrowly confined frequency range, clearly indicating a strong tonal periodicity. The second graph offers insight into the spatial characteristics of the oscillation. It shows that opposing sensors exhibit a phase shift of approximately 180°. However, the pressure distribution cannot be explained by a purely flapping mode—typically characterized by a flip-flop motion of the shear layer—or by a spatially static pressure oscillation, as suggested by the theoretical "static osc" curve. Instead, the spatial phase distribution displays characteristics of a helical mode, as reflected in the "azimuthal mode" theoretical curve. In this case, adjacent sensors detect the 700 Hz pressure oscillation with a phase delay—i.e., the signal arrives at different times around the circumference—indicating the presence of a rotating azimuthal mode with one pressure wave per revolution. Interestingly, the data also suggest a clear directional preference for this helical mode,

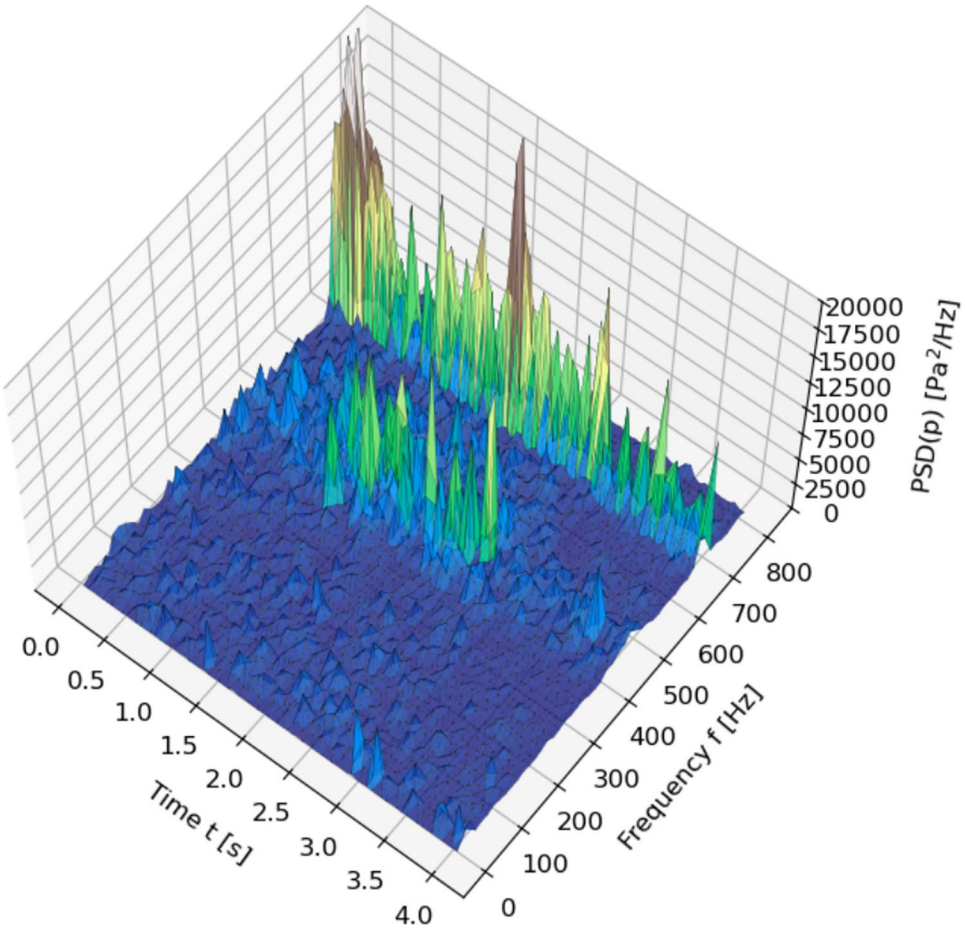

Fig. 5 Close-up of the spectrogram of the base pressure fluctuations for the Mach 0.8-case. Number per segment and number for fast Fourier transform are 1024, while applying a Tukey window with shape parameter of 0.25

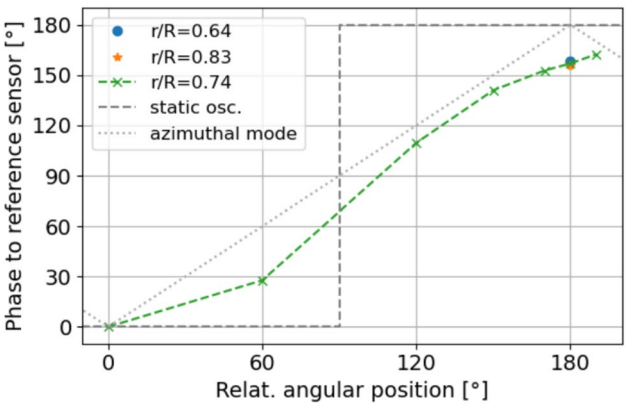

Fig. 6 Pressure phase interdependence of the pressure transducers on the face plate for the Mach 0.8-case

which is somewhat unexpected. In an ideal, perfectly symmetrical setup, no particular direction should be favored, and the rotation direction would be expected to fluctuate stochastically. However, such a directional bias could impose angular momentum on the wind tunnel model or, in a real-world scenario, on the vehicle. This behavior can likely be attributed to minor misalignments in the experimental setup. Even small asymmetries can introduce a preferred orientation in such a dynamic and inherently unstable system—similar to how slight perturbations determine the rotation direction of a vortex in a draining sink. Despite careful setup and alignment, it is practically impossible to eliminate all sources of asymmetry in an experimental environment.

This excitation represents a clear deviation from the findings reported in Saile (2019a) for Mach 0.8. In that study, oscillations around ~ 700 Hz were observed in the absence of a jet, but they vanished once a cold jet was introduced. Instead, a strong amplification appeared at approximately ~ 1400 Hz. Furthermore, Saile (2019a); Saile and Gülhan (2021) proposed a working hypothesis to explain the prominence of this higher frequency. The authors suggested a coupling mechanism between near-wake flow modes and jet screech, specifically involving the symmetric swinging mode of the jet. In contrast, the present case exhibits excitation at roughly half that frequency. This lower frequency is commonly associated with the flapping mode—an asymmetric oscillation arising from the interaction of the shear layer emanating from the upstream shoulder region. As discussed earlier, this mode in the current setup appears to adopt a

helical form, representing a superposition of azimuthal and lateral motions. This observation raises the question of whether a similar resonance phenomenon occurs here as in the prior studies. As noted in Saile (2019a); Saile and Gülhan (2021), jet screech can serve as a counterpart or indicator of resonance. Therefore, within this context, the presence or absence of a screeching frequency may provide insight into the existence of a resonance mechanism in the hot jet configuration investigated here.

The screeching frequency is not easily accessible and its calculation involves considerable uncertainties for the present configuration, especially because the shock cell length of the jet must be estimated. Although the shock topology is shown in Fig. 13, it does not fully capture the shock structure. Additionally, the hot region—affected by turbulence and image overexposure—prevents extraction of detailed features. An extrapolation of the outer shear layer suggests a shock cell length of approximately $1.1 \times D$, with an uncertainty of about $\pm 0.1 \times D$. Using a jet velocity of 2368 m/s (±5%), an ambient flow velocity of 265.2 m/s (±2.5%), and a sonic velocity of 321.1 m/s (±1%), the screeching frequency is predicted as $f_s = 691.0$ Hz with an uncertainty of ±183.6 Hz. These error margins are based on previous measurements or reasonable estimates.

The result is shown in Fig. 7, alongside the "cold jet" condition discussed in Saile (2019a); Saile and Gülhan (2021). It is evident that the increased shock cell length—caused by the higher combustion chamber pressure—shifts the screeching frequency significantly, from about 1400 Hz down to approximately 700 Hz. This suggests that the screeching mode, which was previously coupled with the swinging mode in the "cold jet" case, is now, resonating with the superimposed helical flapping mode.

As a final remark on the pressure spectrograms, it is worth noting the appearance of another frequency in Fig. 5 during motor operation, emerging after about 1 s at approximately

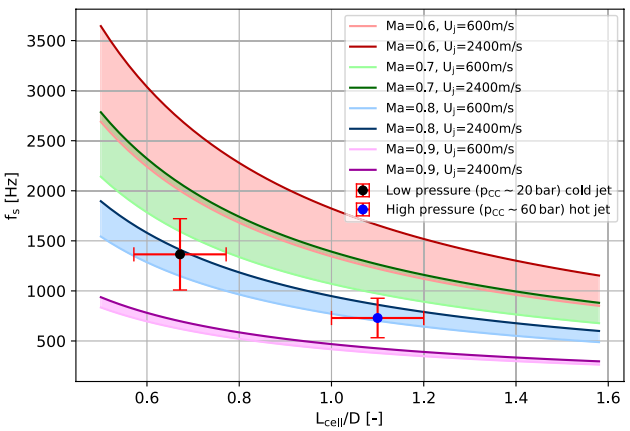

Fig. 7 Screeching frequencies as function of the Mach number, the jet velocity, and the length of the first shock cell for the current setup

470 Hz ($Sr_D = 0.12$). This excitation is not present in all pressure signals but is detected only by two neighboring sensors. A similar frequency was also observed in the cold jet test case reported in Saile (2019a). The origin of this frequency remains unclear and is not investigated further here. It could potentially be related to the aforementioned slight misalignment; however, confirming this hypothesis would require a dedicated study beyond the scope of this work. Additionally, note that the Mach 0.8-case shown in Fig. 4 does not exhibit amplified oscillations near 1400 Hz. This contrasts with previous findings (Saile 2019a; Saile and Gülhan 2021), where a strong coupling between screeching and swinging modes was observed. Nevertheless, as will be demonstrated below, this frequency does influence the shear layer motion and contributes to the excitation of the jet.

Next, the region downstream of the base face plate is discussed. Optical measurement techniques are used to capture the flow dynamics in this area. It is important to note that these measurements rely on the line-of-sight principle or capture data within a plane illuminated by a laser sheet. In other words, it should be emphasized that superimposed flapping or helical modes appear as two-dimensional patterns in these measurements, making it impossible to isolate fully three-dimensional motions, such as true helical flow, using these approaches.

The motion in the base region farther downstream from the base is examined using particle image velocimetry. Due to the distinct excitation observed, the analysis primarily focuses on the Mach 0.8-case, with an emphasis on the unsteady behavior. Accordingly, Fig. 8 presents (1) a contour plot of the Reynolds shear stress distribution in the near-wake, along with results from a sample taken at the location of maximum shear stress. This sample shows (2) a time series of velocity components in the x- and y-directions, their distributions as (3) histograms, and the corresponding (4) power spectral densities.

First, the Reynolds shear stress distribution (Fig. 8-1) clearly shows that the shear layer separated from the base shoulder dominates the dynamic behavior in the near-wake region, as evidenced by the high Reynolds shear stress levels within its influence. Additionally, the shear layer's activity appears to extend into the adjacent "dead water" area in the base wake along the nozzle, triggering a dynamic response there. The velocity sample (Fig. 8-2) taken from the shear layer reveals strong periodic oscillations in both velocity components, each dominated by a single tonal frequency. This periodicity is so pronounced in the u-velocity that it appears as two distinct "bumps" in its histogram (Fig. 8-3), characteristic of a sinusoidal wave. In contrast, the v-velocity histogram lacks these clear "bumps" because the amplitude varies more from cycle to cycle. Nevertheless, both velocity components oscillate at a distinct frequency, as shown by the power

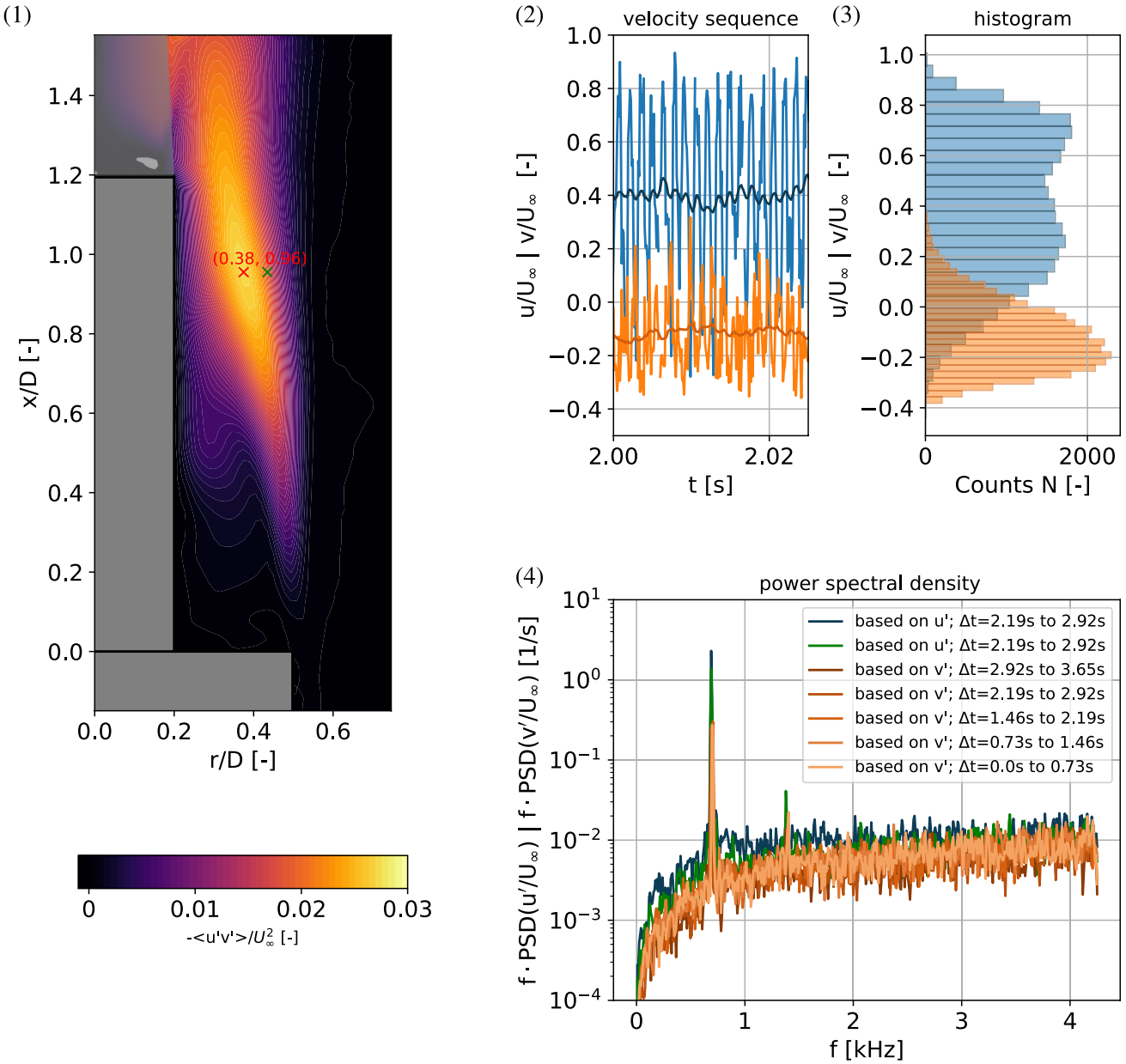

Fig. 8 (1) Contour plot of the Reynolds shear stress distribution -<u'v'> $/U_\infty^2$ in the near-wake and a red cross at the location of minimum Reynolds shear stress, which marks the sampling location for the extracted u- and v-velocity used in the neighboring line plots. (2) Velocity sequence over time of the u- and v-component (blue and orange curve, respectively) and as gliding average over 6 ms (dark orange and dark blue curve, respectively), (3) the u- and v-velocity histogram, and (4) the power spectral density of the sampled u- and v-velocity for different temporal intervals. The curve in green corresponds to the sample taken from the green cross as marked in the contour plot. The ambient flow conditions are set to Mach 0.8

spectral density (Fig. 8-4). Similar to the base pressure signal, the dominant frequency is 700 Hz, corresponding to a Strouhal number of 0.18. All evidence strongly indicates that this frequency is characteristic of the shear layer's flapping motion. It is also important to note that the dynamic behavior in the near-wake is largely independent of the combustion chamber pressure regarding the excited modes: The oscillation frequency remains constant throughout the operation of the solid propellant motor, as illustrated by the representative v'-velocity spectrum.

An additional, lower-amplitude peak appears near the edge of the shear layer (indicated by the green cross in the contour plot). This peak occurs at 1400 Hz, which corresponds to the second harmonic—twice the primary frequency. Its location and the associated Strouhal number of 0.36 suggest that this mode is linked to the shear layer

swinging, representing an intrinsic twisting motion of the shear layer.

The motion of the two dominant frequencies is captured in Fig. 9. It displays the averaged velocity distribution at Mach 0.8 (Fig. 9-1) alongside the power spectral density and phase distributions at 700 Hz and 1400 Hz. The latter two plots are derived from a power spectral density analysis performed at every spatial point based on the PIV data. The motion of the individual modes $U_{f_0}(t)$, oscillating at frequency f_0, can be reconstructed by superimposing the average flow field $\overline{U}$ with the combined amplitude A_{f_0},

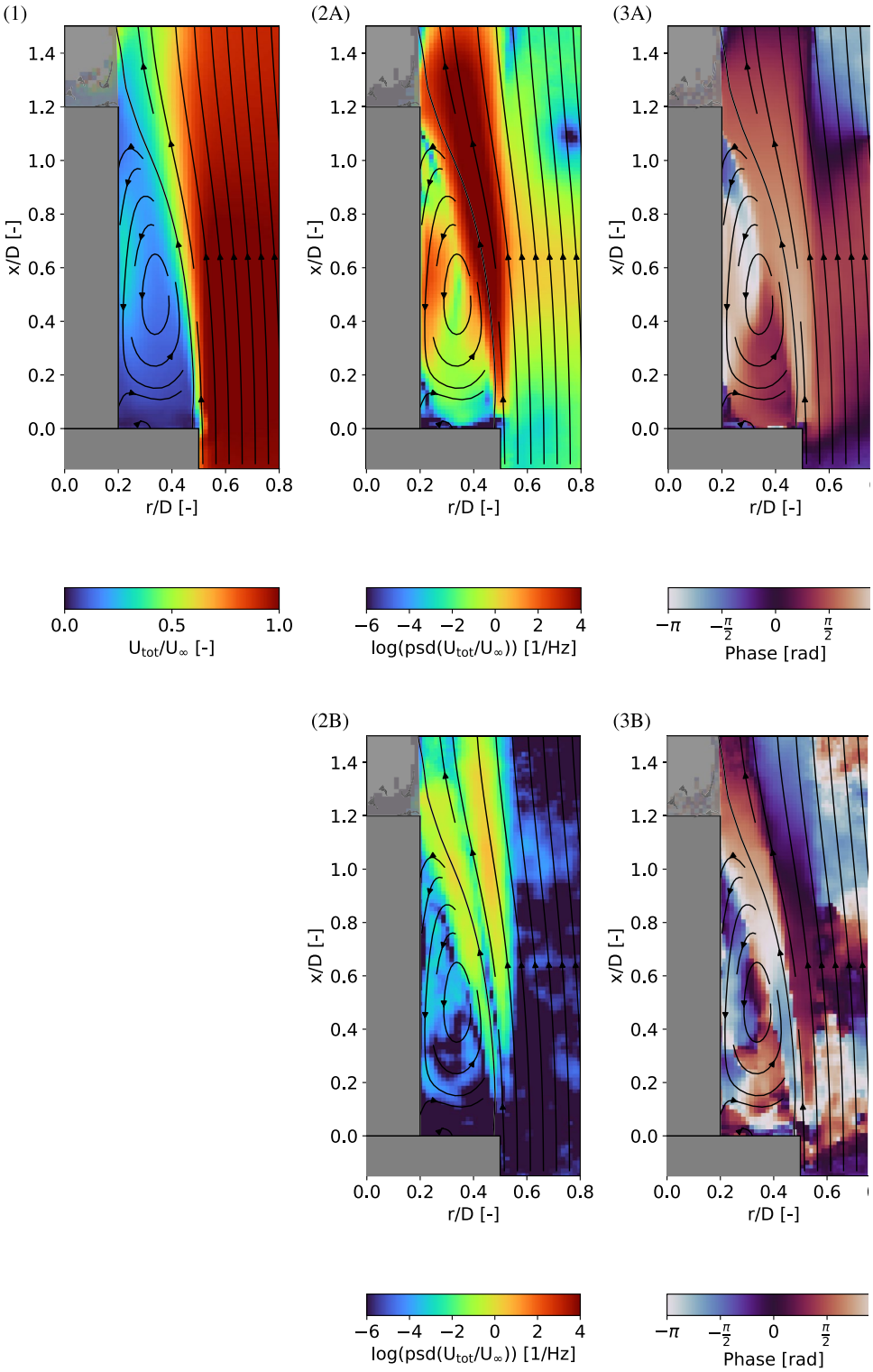

Fig. 9 Average velocity field (1), amplitude (2A and 2B), and phase distribution (3A and 3B) for the Mach 0.8-case as a results of the power spectral density analysis (14000 samples equivalent to 1.65 s). Additionally, the streamlines are plotted in all distributions. The top row corresponds to a frequency of 700 Hz (marked with -A), the bottom row to a frequency of 1400 Hz (marked with -B)

obtained from the power spectral density field $S_{f_0}(f_0)$ and phase field Φ_{f_0}, as detailed below.

$$U_{f_0}(t) = \overline{U} + A_{f_0} \cdot cos(2\pi f_0 \cdot t + \Phi_{f_0}) \tag{3}$$

$$A_{f_0} = \sqrt{2 \cdot S_{f_0}(f_0)} \quad \text{one-sided PSD and real-valued signal} \tag{4}$$

First, the average velocity distribution is discussed (Fig. 9-1). It exhibits the typical characteristics of the near-wake flow field: Separation occurs at the base and develops into a shear layer that, in the case of Mach 0.8, reattaches (on average) near the nozzle exit. Enclosed by the shear layer, the base, and the nozzle surface is the recirculation bubble. This region is typically highly unsteady and contains turbulent structures across a range of scales. In other words, the shown velocity distribution represents an average flow field, and at any given instant, the actual recirculation bubble may differ significantly from this mean state. Furthermore, it is noteworthy that the shear layer—approximated by the stagnation streamline—reattaches, on average, onto the jet. This behavior differs from that observed at other Mach numbers. At Mach 0.6 and Mach 0.7, reattachment occurs exclusively on the solid nozzle wall, whereas at Mach 0.9, it takes place entirely on the jet (Saile et al. 2019c). In contrast, the Mach 0.8-case shows a hybrid reattachment behavior, where the shear layer intermittently reattaches either on the jet or on the solid wall, indicating an interaction between the shear layer and the jet itself.

Next, as a dynamic component superimposed on the average flow field, the power distribution at 700 Hz ($St_D = 0.18$) in Fig. 9-2A highlights the regions that oscillate most intensely at this frequency. These areas are predominantly located along the shear layer. Notably, the stagnation streamline—originating from the separation point at the shoulder—divides this amplified region symmetrically into two sides of approximately equal extent. Additionally, increased sensitivity to oscillations is observed both upstream and downstream of the midpoint along the nozzle surface.

Then, the phase distribution in Fig. 9-3A provides insights into the spatio-temporal characteristics of the flow. Within the recirculation bubble, a phase difference of π is observed between the upstream-directed motion along the nozzle surface and the radial flow along the face plate of the base. In practical terms, an increase in velocity near the nozzle surface at approximately $x/D \sim 1.0$—typically triggered by a large vortex structure (Saile 2019a)—is accompanied by an increase in radial velocity at the base. However, this latter response occurs with a temporal delay of $\Delta t = \frac{1}{2} \cdot \frac{1}{700\,\text{Hz}}$. A similar phase difference of π is evident between this near-nozzle region and the outer shear layer at a radial position of approximately $r/R \sim 0.3$. These two regions are separated by a sharp phase gradient, indicating that increased downstream velocities in the shear layer lag behind the upstream velocities along the nozzle surface by the same time interval, $\Delta t = \frac{1}{2} \cdot \frac{1}{700\,\text{Hz}}$. Within the shear layer itself, there is a downstream phase stratification of approximately $\pi/2$. This means that when the velocity near the reattachment point is relatively high, it is relatively low at the same moment in time directly downstream of the shoulder separation. Additionally, large-scale structures are visible in the outer flow field, suggesting that the near-wake dynamics influence the free-stream region. These disturbances exhibit characteristic spatial scales that depend on both frequency and free-stream velocity. The corresponding characteristic length scale can be estimated as $L_{700\,\text{Hz}}/D = U_\infty/f_{700\,\text{Hz}}/D$. In the free-stream region ($r/D > 0.5$), a structure with a length of approximately 1.2 to 1.3 is visible, which corresponds closely to one-quarter of the calculated characteristic wavelength ($\sim 5.6/4 = 1.4$).

The power density distribution at the higher harmonic frequency of 1400 Hz (Fig. 9-2B) also highlights the shear layer as the region of dominant activity. However, unlike the lower-frequency mode, this distribution emphasizes areas both inside and outside the stagnation streamline emanating from the base. This explains why the 1400 Hz component is only weakly represented in the power spectral density at the location of maximum Reynolds shear stress (see Fig. 8). This mode introduces an additional velocity component to the mean flow and is characterized by a phase difference of π across the stagnation streamline, as well as a phase shift of π between the vicinity of the separation point and the region near reattachment. These phase relationships (Fig. 9-3B) reveal the typical intrinsic twist of the swinging mode within the shear layer, which propagates downstream, as indicated by the observed downstream phase stratification. In general, the contribution of this higher harmonic to velocity fluctuations within the recirculation bubble appears relatively small compared to the dominant influence of the flapping shear layer mode. However, one notable observation is its effect on the free-stream flow: The higher frequency leads to a corresponding reduction in the spatial scale of the induced fluctuations. As expected from spatio-temporal scaling, the wavelength associated with this 1400 Hz mode is approximately half that of the flapping mode at 700 Hz.

The preceding discussion captures the key characteristics of the dominant flow modes; however, their physical interpretation may remain somewhat abstract. To provide a more intuitive understanding, the modes are reconstructed and illustrated as temporal cycles in Fig. 10 and Fig. 11, corresponding to the dominant frequencies of 700 Hz and

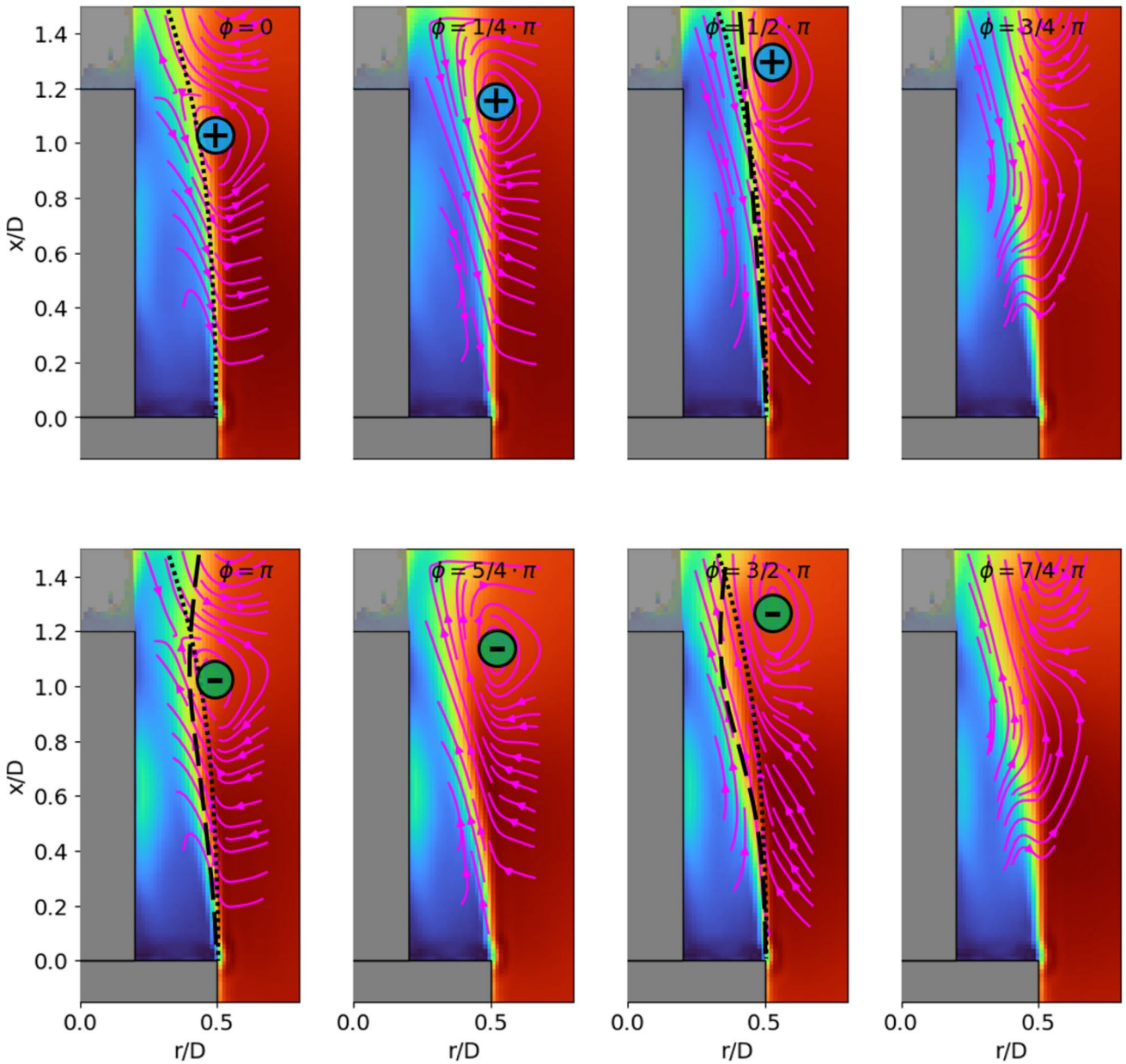

Fig. 10 Visualization of the flapping mode at 700, Hz obtained via PIV. The contour plots show the superposition of the averaged flow field and the oscillation field, while the streamlines depict only the recombination of the psd and the phase field (mode only, without mean flow superposition). The black dashed line denotes the reference shear layer position at phase $\Phi = 0$. The black dotted line indicates the instantaneous shear layer position at the respective phase and is shown only in panels where the superposition produces a sufficiently large displacement to allow a clear visual distinction. In phases where the instantaneous and reference shear layer positions are nearly coincident, the dotted line is omitted to avoid visual clutter. The eight panels represent eight equidistant phases of the oscillation cycle, separated by $\Delta\Phi = \pi/4$. Oscillation field components inducing clockwise and counterclockwise vorticity are marked by minus and plus symbols, respectively

1400 Hz, respectively. In these visualizations, only the oscillatory component of each mode is shown (i.e., without the superposed mean flow). Streamlines are included to highlight the local flow structures associated with each mode. Additionally, symbols indicating the rotational direction of vortices—counterclockwise (+) and clockwise (−)—are annotated to aid interpretation. Dashed lines are also sketched to approximate the instantaneous position of the shear layer.

The reconstruction of the dominant mode at 700 Hz, shown in Fig. 10, combines the power density and phase information to reveal downstream-propagating vortices that

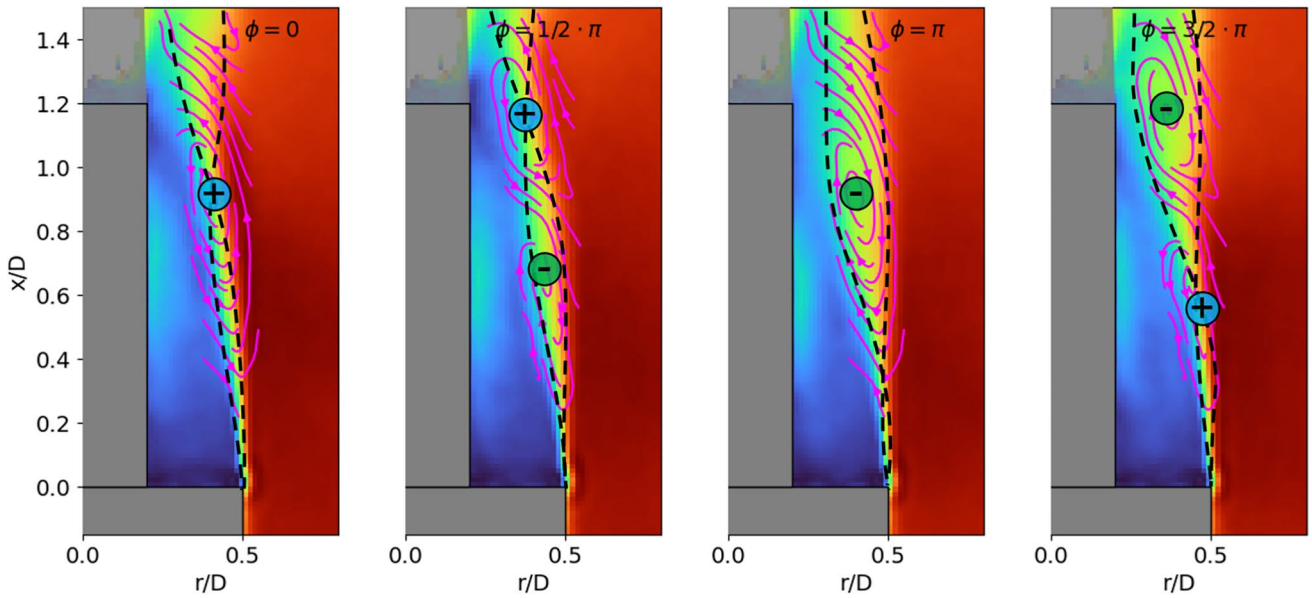

Fig. 11 Visualization of the swinging mode at 1400 Hz obtained via PIV. The contour shows a superposition of the averaged flow field and the oscillation, while the streamlines depict only the recombination of the psd and the phase field (without superpositioning, ergo mode only). The black dashed line sketches the impact onto the shear layer, referring to the shear layer thickness modulation in the downstream direction. The four images correspond to four phases ($\Phi = 0, \Pi/2, \Pi, 3/2\Pi$) in a cycle. Oscillation field components that induce clockwise and counter-clockwise rotating vorticity are marked with a plus and minus sign, respectively

modulate the shear layer dynamics. Vortices with negative vorticity (−) enhance the velocity near the nozzle or jet, drawing the shear layer closer to the centerline. Conversely, vortices with positive vorticity (+) have the opposite effect, pushing the shear layer away from the centerline. This alternating influence describes the characteristic flapping motion of the shear layer.

The reconstruction of the second harmonic, shown in Fig. 11, also reveals downstream-propagating vortices superimposed on the mean flow field. However, this mode exhibits a characteristic wavelength that is half that of the primary mode. Notably, the vortices act directly along the stagnation streamline of the shear layer emerging from the base shoulder. As a result, the shear layer either thickens or thins, depending on the vorticity: Negative vorticity leads to thickening, while positive vorticity results in thinning. This dynamic creates the impression of downstream-traveling bulges and imparts a twisting motion to the shear layer—an indicator of the characteristic swinging behavior. Given the planar nature of the visualization, it remains unclear whether the observed motion is purely two-dimensional or a result of a combination of modes. However, the pressure phase diagram in the azimuthal direction on the face plate (see Fig. 6) suggests the presence of a helical mode. This implies that the motion depicted in Fig. 11 may also stem from a rotating and swinging shear layer.

For the sake of completeness—and to facilitate comparisons across the different Mach number cases, while also highlighting the consistency of the results—the velocity spectrum is shown for all investigated Mach numbers. It is important to note that selecting an appropriate sampling point for such comparisons is non-trivial, as it strongly depends on the dominant features of the flow field (see Fig. 9-2A and Fig. 9-2B). Therefore, the sampling point is chosen based on a flow characteristic—specifically, the location of maximum Reynolds shear stress within the shear layer. The corresponding coordinates for each case are listed in Tab.1. This table further underscores the distinctive nature

Table 1 Position of maximum Reynolds shear stress level in the shear layer, which was used to extract the velocity sample for the spectrum shown in Fig. 12

Ma_{nom}	0.6		0.7		0.8		0.9	
jet	off	on	off	on	off	on	off	on
x/D	0.89	0.92	1.02	0.98	1.15	**1.02**	1.22	1.25
r/D	0.35	0.35	0.33	0.35	0.34	0.37	0.35	0.35

of the Mach 0.8-case, which also stands out in terms of the shear layer reattachment behavior, referred to as hybrid reattachment. Table 1 shows that the location of maximum Reynolds shear stress generally shifts downstream with increasing Mach number in both configurations: with and without an operating jet. However, this trend is relatively weak, with one notable exception—Mach 0.8. In this case, the reference point is markedly shifted upstream. This deviation is likely attributable to the jet acting as an effective ejector pump, thereby enhancing the potential for tension buildup and release within the shear layer.

Turning to the power spectrum of the velocity in the shear layer, Fig. 12 reveals that distinct oscillations are primarily observed at Mach 0.8 and Mach 0.9 in the case without a jet, and at Mach 0.8 when the jet is operating. For all other cases, the spectrum remains relatively flat. This flatness can be attributed to the fact that mutual interaction of the shear layers is impeded—either by the geometry, namely the solid surface of the nozzle, or by the presence of the jet itself. In the cases without a jet at Mach 0.8 and Mach 0.9—where the shear layer extends beyond the nozzle length (Saile et al. 2019c, b; Saile et al. 2021; Saile 2019a)—distinct peaks appear in the spectrum at 713.9 Hz and 780.3 Hz. These correspond to a non-dimensional frequency of $St_D = 0.18$, which is characteristic of flapping motion. Interestingly, for Mach 0.9, this excitation vanishes when the jet is activated, supporting the earlier assertion that a jet suppresses mutual shear layer interaction. In contrast, a strong amplification is observed at Mach 0.8 with an operating jet. This is attributed to a resonance phenomenon involving screeching (see Fig. 7).

The motion of the jet is analyzed using schlieren imaging results. Figure 13 presents three images for Mach 0.8: an instantaneous snapshot (left), a time-averaged schlieren image (center), and a standard deviation map (right) showing intensity fluctuations. The averaging and standard deviation calculations are based on a dataset of 17000 images, recorded during the phase when the combustion chamber pressure is at its peak (5.8 MPa $\leq p_{CC} \leq$ 6.2 MPa).

The instantaneous schlieren image reveals strong gradient patches, indicating turbulence in the wake. The most prominent density gradient fluctuations appear in the jet's shear layer, which envelops the jet like a jacket. Additionally, the jet is visibly deflected to the right at this instant (indicated by a white right-pointing arrow in the upper part of the image). In an image sequence or video (not shown here), an alternating left-right motion is evident. Finally, this frame also captures a feature typically associated with an acoustic upstream-traveling wave (marked by a white arrow indicating the direction of propagation, framed by two red arrows, and labeled as "wave"). Such waves are characteristic of jet screech (Powell 1953a, b) and have also been observed in rocket wake flows (Saile and Gülhan 2021; Saile 2019a).

On average, the supersonic jet is aligned with the centerline (middle image). This image also reveals the shock structures commonly observed in exhaust jets: a lip shock at the nozzle exit, a Mach disk farther downstream (tracked in Fig. 19), and a shock reflection of the incipient lip shock at the Mach disk. Additionally, the image outlines the evolving shear layer along the jet boundary. The standard deviation image (right) provides insight into the spatial distribution of fluctuations, highlighting the strongest regions. The most intense fluctuations occur near the jet deflection observed in the instantaneous image, at approximately $x/D \sim 2.5$. Increased fluctuations are also visible near the nozzle lip within the shear layer.

For Mach 0.8, the schlieren images revealed an alternating motion of the jet outline. To track this modulation, the intensity values of a single pixel in the shear layer at $[r, x]/D = [-0.3, 2.2]$ were extracted over time and analyzed for their spectral content (Welch 1967). The power spectral density shown in Fig. 14 confirms this oscillatory behavior, showing strong peaks at $f = 702$ Hz ($St_D = 0.18$) and at 1400 Hz ($St_D = 0.36$). Moreover, the graph indicates that this

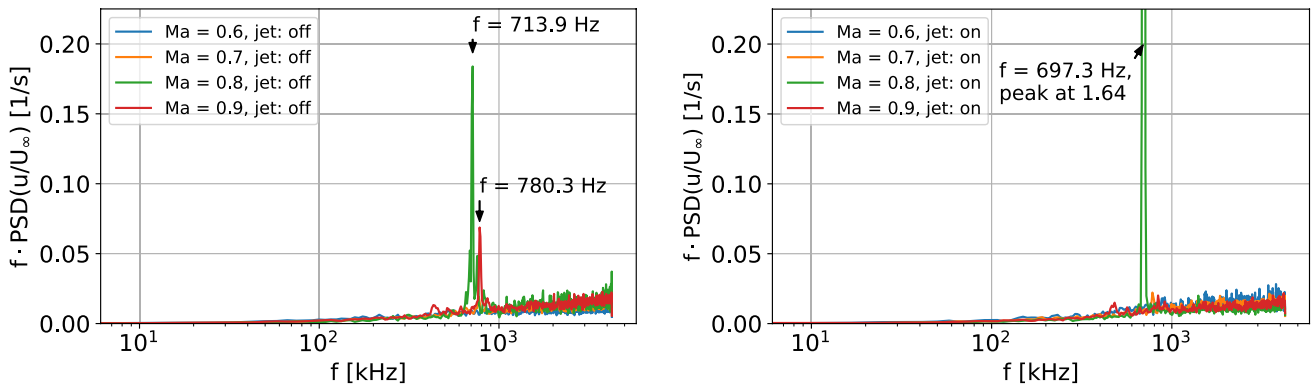

Fig. 12 Power spectral density of the streamwise velocity extracted from the coordinates as given in Tab. 1. In the left graph, the jet is off, while it is operating in the right graph

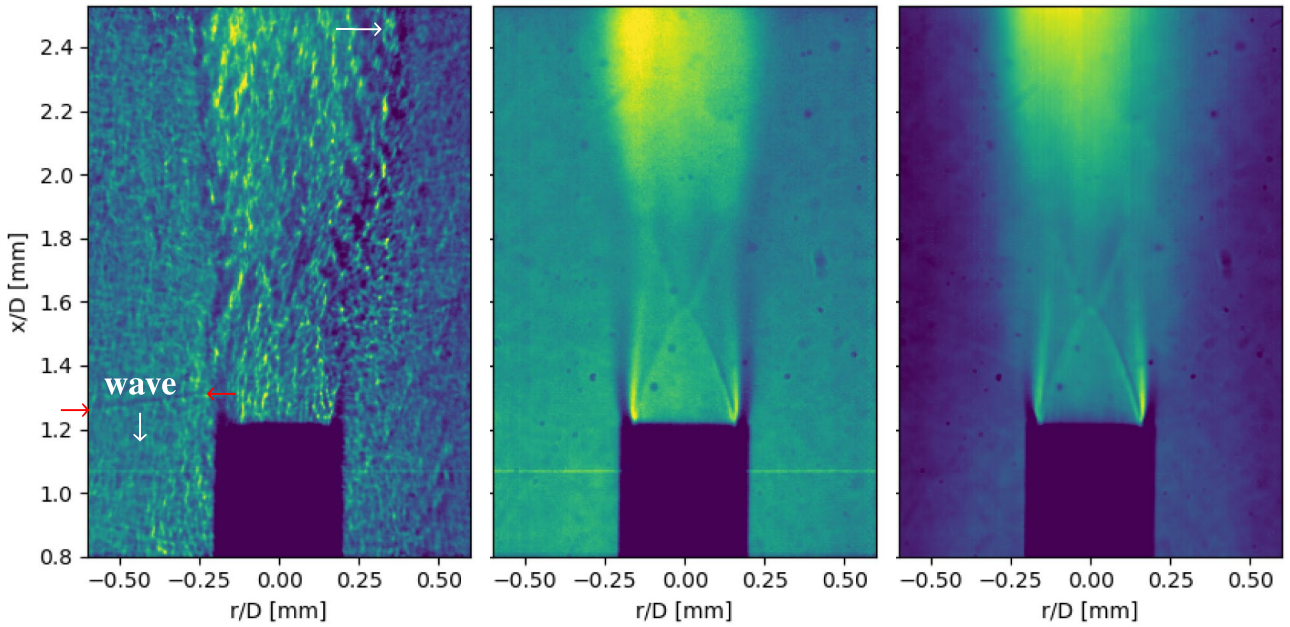

Fig. 13 Instantaneous (left), averaged (mid), and standard deviation (right) of high-speed schlieren recordings of the base flow and the jet (average and standard deviation of 17000 images) at Mach 0.8

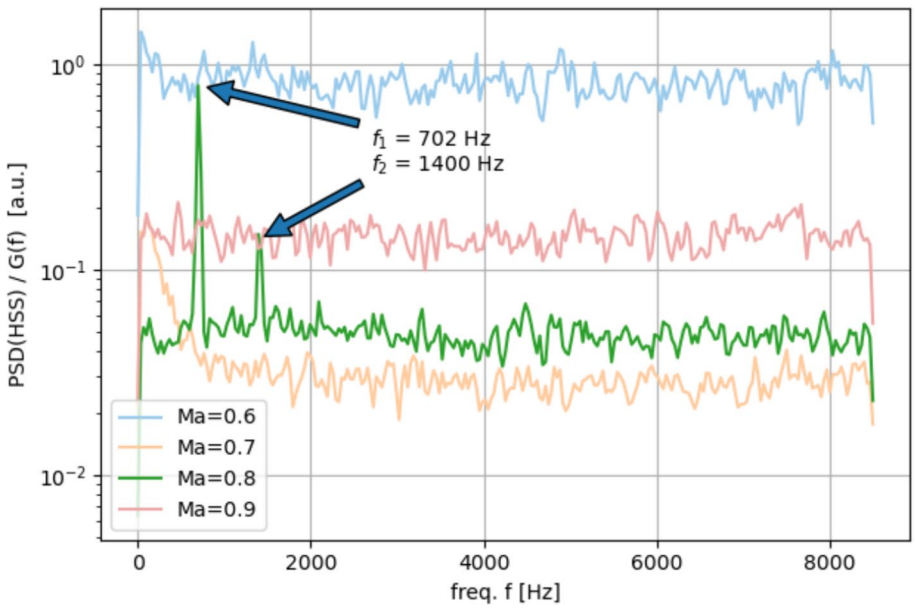

Fig. 14 Power spectral density (Welch's method(Welch 1967), 512 samples per segment, 50% overlap) of the brightness fluctuation of a pixel located at $[r, x]/D = [-0.3, 2.2]$

oscillation is specific to Mach 0.8. For other Mach numbers, the motion is either negligible or absent in the data, consistent with the spectral findings from the pressure signal in Fig. 4 and the velocity signal in Fig. 12.

As with the PIV dataset, a spectral analysis is applied here to all pixels of the recording for the Mach 0.8-case, where oscillations are most pronounced (Fig. 14). Accordingly, Fig. 15 presents the amplitude and phase of the high-speed schlieren fluctuations in the base region, obtained from a power spectral density analysis. Clear structures emerge in both amplitude and phase for the two dominant frequencies, namely $f = 702$ Hz and $f = 1400$ Hz. While the phase diagrams illustrate the nature of the periodic oscillations, the amplitude diagrams reveal their spatial prominence.

The oscillation at $f = 702$ Hz exhibits antisymmetry about the axis, whereas the higher frequency at $f = 1400$ Hz displays a symmetric oscillation. Unlike the PIV dataset, schlieren imaging offers optical access to both sides of the

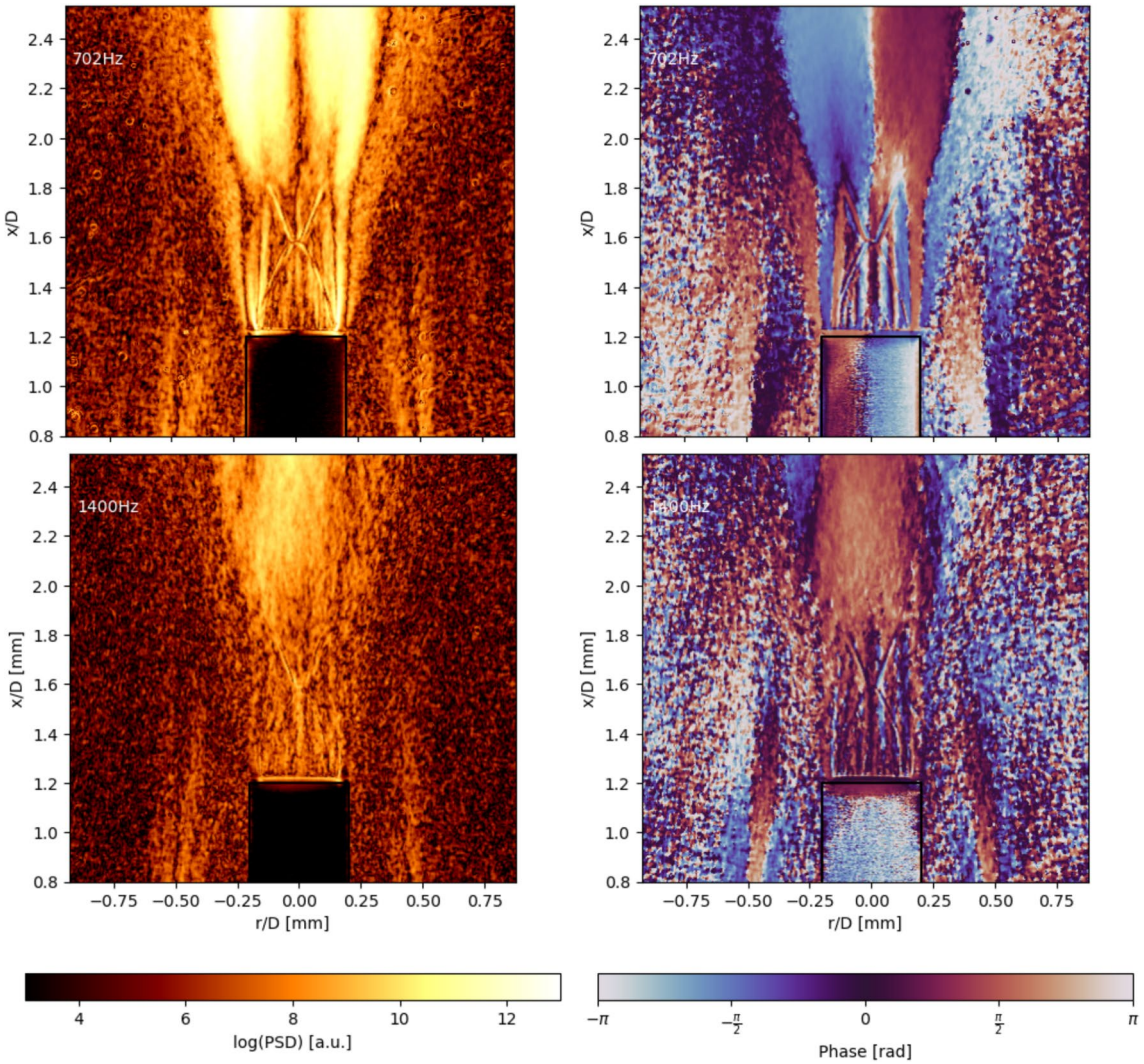

Fig. 15 Amplitude (left) and phase (right) of the high-speed schlieren fluctuations analyzed retrieved from a power spectral density analysis in the base region between $t = 1.5$ s and 2.5 s after the ramp up of the rocket motor (combustion chamber pressure $p_{CC} \sim 6$ MPa) at the frequency $f = 702$ Hz (top) and 1400 Hz (bottom)

symmetry axis, allowing for an unambiguous identification of whether a mode is symmetric or antisymmetric. The lower-frequency mode has its strongest impact near the second cell of the jet shock train, downstream from $x/D = 1.8$. Additionally, both modes exhibit features upstream of the nozzle exit in the region associated with the shear layer that evolves from the flow separation at the base (at $r/D = \pm 0.5$). In other words, Fig. 15 bridges the wake and the jet flow, illustrating how jet flow excitation and decay interact with the upstream wake flow.

As discussed above, the phase distribution combined with the power spectral density (PSD) field effectively captures the spatio-temporal behavior of the flow. To provide a more intuitive understanding, these effects are visualized through reconstructions shown in Fig. 16 and Fig. 17 for the flapping and swinging modes, respectively. The flapping motion of the shear layer induces a corresponding side-to-side oscillation of the jet and its shear layer, as illustrated in Fig. 16. This motion could also represent a helical mode (as suggested in Fig. 6), although this cannot be distinguished clearly due to the line-of-sight nature of the schlieren imaging. The higher-frequency mode reconstruction in Fig. 17 shows an oscillating growth and decay in the radial direction. Overall, these jet dynamics likely contribute to decay of the jet train, ultimately producing upstream-traveling pressure waves (Powell 1953a, b; Poldervaart 1974; Poldervaart et al. 1969; Tam et al. 1986; Raman 1998), possibly caused by shock leakage. Note that shock leakage (Manning and Lele 1998, 2000; Edgington-Mitchell et al. 2021; Edgington-Mitchell 2022) is the process by which unsteady shock shear layer interactions in a supersonic jet allow upstream-propagating acoustic pressure waves to escape from the shock cell structure through the shear

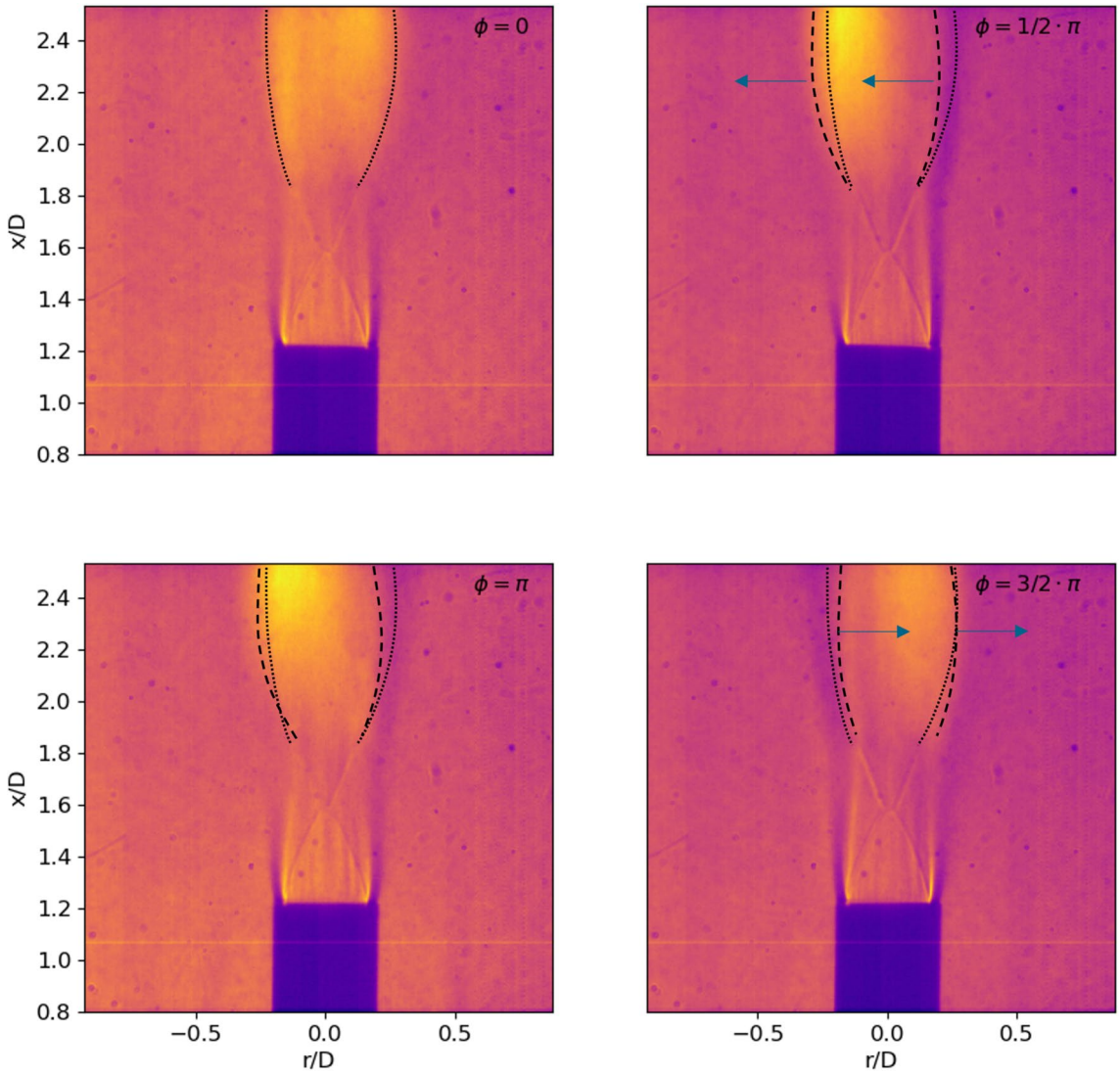

Fig. 16 Reconstruction of the high-speed schlieren spectral analysis visualizing the impact of one cycle (at phase $\Phi = 0, 1/2\pi, \pi, 3/2\pi$) of the flapping mode ($f = 700\,\text{Hz}$ / $\text{St} = 0.18$) on the jet. The dashed and dotted lines outline the silhouette of jet with the dotted line for $\Phi = 0$ acting as reference

layer, thereby enabling acoustic feedback and resonance phenomena such as jet screech.

4 Key finding—the schematic model

In Saile and Gülhan (2021); Saile (2019a), and as outlined in the introduction, a hypothesis was proposed to explain the strong amplification of oscillations in the base region of space launchers within the transonic flow regime. It suggested that this amplification results from an interaction between near-wake instabilities and jet screech. The hypothesis was based on experiments conducted with cold jets at low chamber pressures. Due to the low chamber pressure—used to prevent condensation in the jet caused by the cold chamber temperature—the resulting shock cell length was shorter. Consequently, jet screech occurred at higher frequencies and coupled with the swinging mode.

In contrast, for hot jets at high chamber pressure, jet screech shifts to lower frequencies. In this case, it resonates with the asymmetric flapping mode, which is the mode observed in flight for Ariane 5. This experimental setup therefore reproduces flight-representative conditions. Moreover, the findings further support the schematic model introduced in Saile and Gülhan (2021); Saile (2019a), extending it to include the coupling between the asymmetric flapping mode and jet screech. A visualization of this extension is shown in Fig. 18.

The self-exciting cycle for the symmetric coupling can be divided into four interdependent phases. A similar sequence

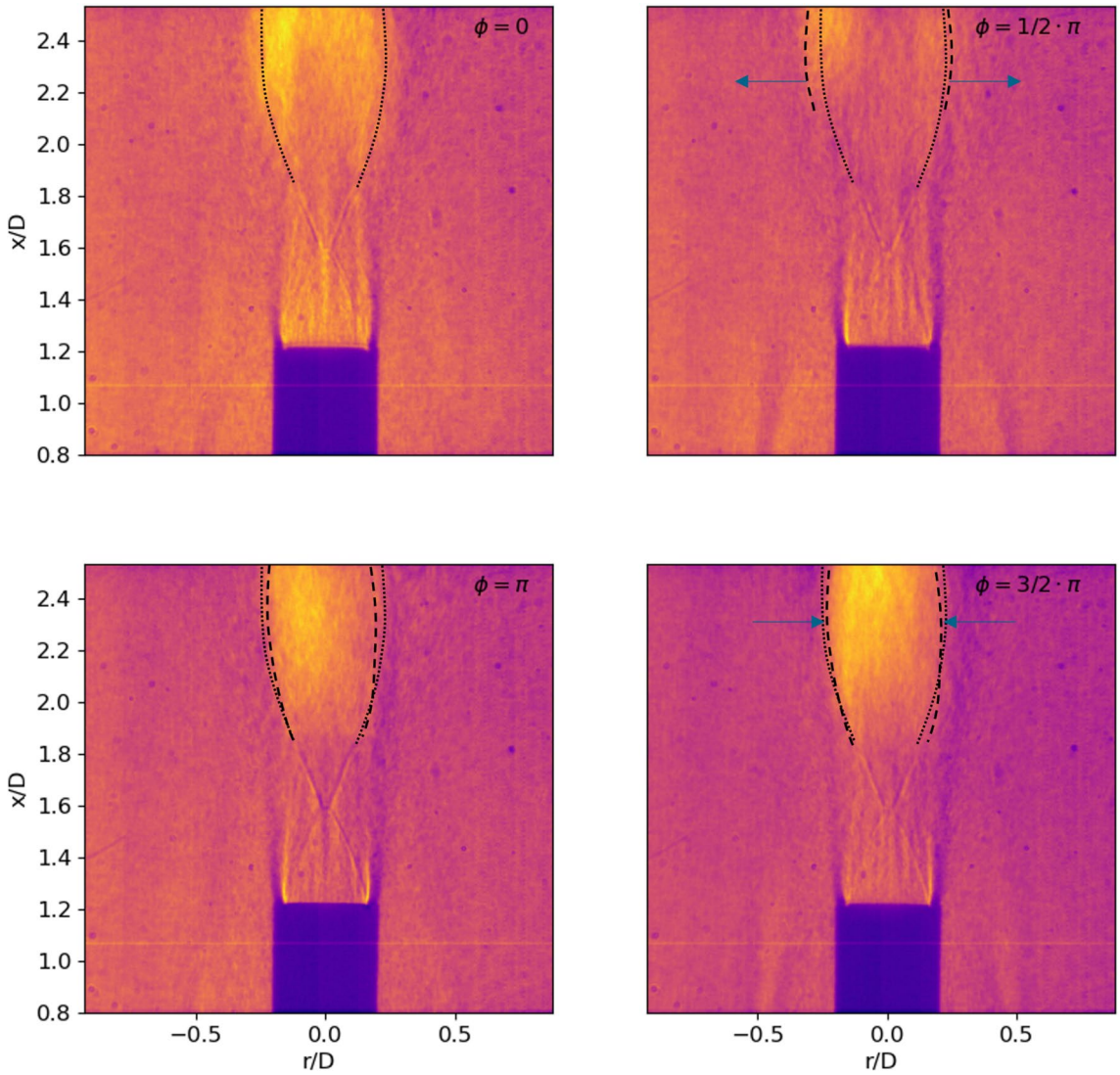

Fig. 17 Reconstruction of the high-speed schlieren spectral analysis visualizing the impact of one cycle (at phase $\Phi = 0, 1/2\pi, \pi, 3/2\pi$) of the swinging mode ($f = 1400\,\text{Hz}$ / $\text{St}_\text{D} = 0.36$) on the jet. The dashed and dotted lines outline the silhouette of jet with the dotted line for $\Phi = 0$ acting as reference

is observed in the case of asymmetric coupling; however, the effects on either side of the symmetry line are phase-shifted by half a period. Aside from this shift, the chain of cause and effect remains unchanged:

1. **Sound wave generation:** This phase mirrors the mechanism responsible for jet screech. As a turbulent structure in the shear layer convects past the shock cells, it generates a pressure wave that radiates in all directions.
2. **Upstream propagation:** Of particular relevance is the upstream-propagating portion of this pressure wave, which travels back toward the nozzle.
3. **Recirculation bubble response:** The arriving pressure wave causes the recirculation bubble at the nozzle base to grow, eventually leading to the shedding of a vortex from the nozzle lip.
4. **Vortex feeding:** This vortex is then entrained into the shear layer of the jet as a new turbulent structure, closing the feedback loop by serving as the source for the next pressure wave generation (returning to phase 1).

This self-sustaining feedback mechanism closely resembles the classical screech tone excitation process. However, rather than relying on an aeroacoustic feedback loop at the nozzle lip, the vortex shed from the recirculation bubble serves as the primary disturbance reintroduced into the cycle. In the symmetric case, the upstream-traveling pressure waves are illustrated as arriving at the base plate without a phase

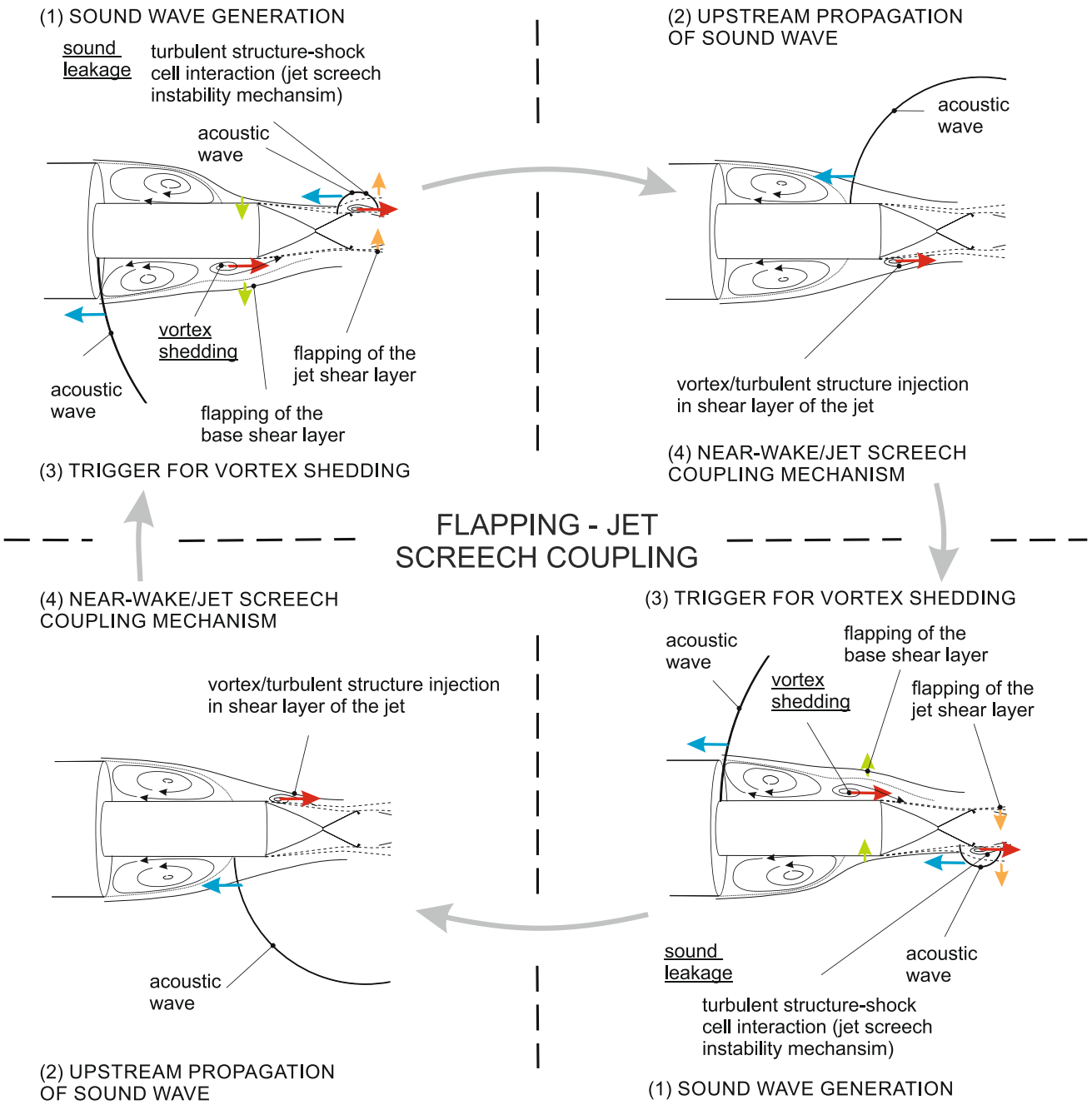

Fig. 18 Schematic model of the flapping—jet screech feedback loop

difference, consistent with observations of the screech tone behavior.

5 Conclusion

This study set out to investigate whether experiments using a high-pressure, high-temperature exhaust jet could faithfully replicate real flight conditions and capture the aerodynamic phenomena responsible for the excessive loads experienced in the base region of Ariane 5 Flight 157. Specifically, it aimed to validate the hypothesis—derived from prior cold-flow studies—that a resonance mechanism between near-wake instabilities and jet screeching contributes significantly to base region buffeting under flight-like conditions.

These research questions were experimentally addressed in the subsonic flow regime using the vertical test section (VMK), where a hot exhaust jet, produced by a combustion chamber operating at approximately 60 bar and 2560 K, simulated the conditions of real flight. Flow dynamics

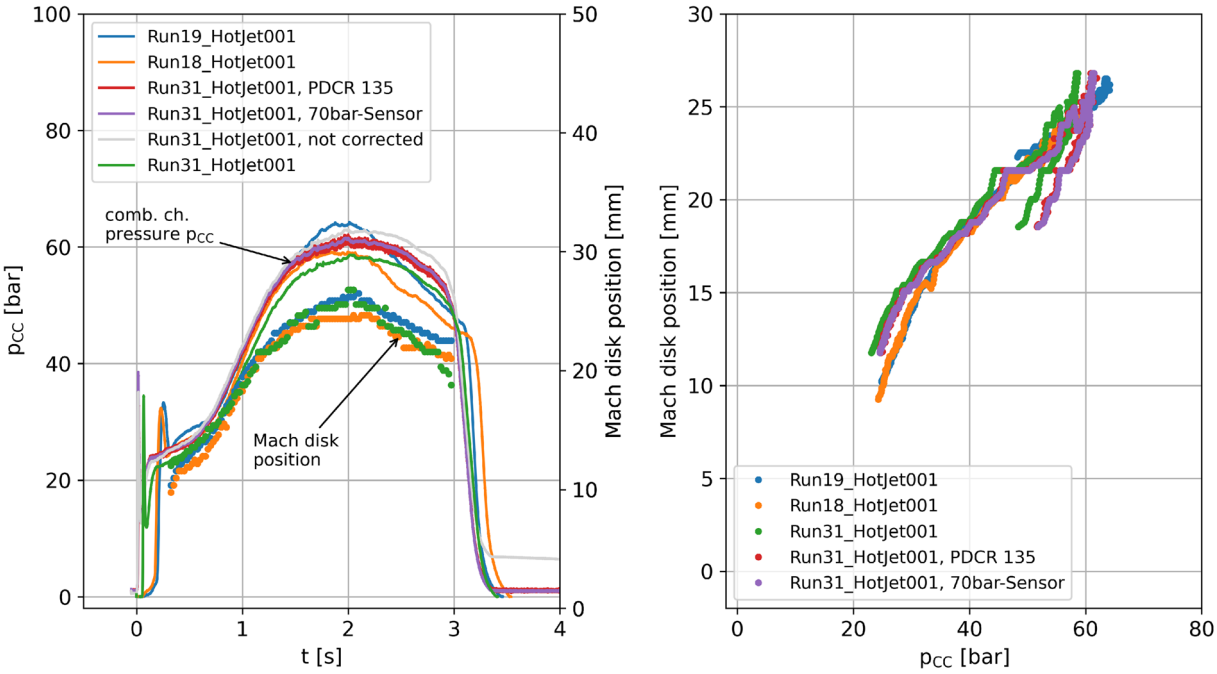

Fig. 19 Evolution of combustion chamber pressure (1) and location of the Mach disk (1 & 2) measured from the nozzle exit

were captured using time-resolved high-speed schlieren imaging, high-speed particle image velocimetry (PIV), and fast-response Kulite pressure sensors. Spectral analysis of the measurement data provided detailed insights into the spatio-temporal evolution of the flow field.

The results confirmed that the dominant excitation modes in the base region are associated with two key aerodynamic instabilities: flapping (asymmetric) and swinging (symmetric). Importantly, the flapping mode was shown to enter resonance with jet screeching at Mach 0.8, resulting in strong, alternating pressure oscillations. This finding substantiates the hypothesis that such resonance can significantly amplify unsteady loads, offering a plausible explanation for the structural stresses observed during the Ariane 5 failure.

The spatial distribution of excited regions, resolved at dominant frequencies, revealed the location and structure of the most active flow zones, extending from the base plate across the near-wake region and laterally along the nozzle and exhaust jet. Modal reconstruction further illustrated the evolution and decay of the shear layer, highlighting its role in the hybrid reattachment process and in shaping jet dynamics. These results show that the previously identified excitation mechanisms in cold-flow tests remain valid under hot jet conditions.

Moreover, the findings enabled an extension of the previously developed schematic model (Saile and Gülhan 2021; Saile 2019a). While the original model focused on symmetric interactions and their coupling with jet screech, the current results reveal that the same feedback principles apply to the asymmetric flapping mode. The model has thus been expanded to describe the full feedback loop involving asymmetric flapping and jet screech, incorporating the observed phase relationships and spatial mode distributions. This extension reinforces the generality of the underlying excitation mechanisms and provides a unified framework for interpreting both symmetric and asymmetric base flow oscillations in transonic jet environments.

Crucially, all diagnostic techniques consistently captured the same physical phenomena, providing a comprehensive and coherent picture of the flow field. The strong agreement across all measurement modalities reinforces the robustness of the experimental approach.

Finally, the study not only explains the unsteady aerodynamic loads observed during Ariane 5's subsonic flight regime but also provides practical insights for mitigating buffeting—most notably by shortening the nozzle to prevent hybrid shear layer reattachment. These findings directly contribute to improving predictive models and advancing the design of safer, more robust launch systems.

Appendix—Chamber pressure & Mach Disk

A brief excursus is provided here to highlight the implications of using a small-scale rocket motor for testing purposes. The solid rocket motor serves primarily as a means to generate a hot exhaust jet, enabling investigation of base flow interactions under realistic conditions. One clear

advantage is the ability to achieve flight-relevant exhaust properties, with combustion chamber temperatures around 2560 K and exit velocities on the order of 2400 m/s. However, this setup also introduces certain limitations: Notably, the combustion chamber exhibits a transient pressure evolution, and the available testing time is relatively short.

Figure 19-1 displays the combustion chamber pressure evolution for three different tests, recorded using three different pressure sensors. Following ignition, the chamber pressure rises from an initial value of approximately ~ 20 bar to a peak of around ~ 60 bar, before decreasing during the tail-off phase after roughly ~ 3 s. The pressure evolution is highly repeatable, with deviations within an error margin of $\pm 5\%$, and the readings from the different transducers are in good agreement. However, it should be noted that the Kulite sensor exhibits a drift over time, as it does not return to the ambient pressure level after shutdown. This behavior is attributed to thermal effects and is compensated for by assuming a constant drift offset. Unless otherwise stated, the analyses are based on data extracted from the interval $1.5\,\text{s} \leq t \leq 2.5\,\text{s}$, during which the pressure remains relatively stable, forming a plateau.

As an additional characterization of the hot jet, the location of the Mach disk—identified through schlieren measurements and discussed in the context of Fig. 13 (e.g., center image)—was tracked throughout the test. With increasing combustion chamber pressure, the Mach disk is observed to shift further downstream. This relationship is illustrated in Fig. 19-2, which correlates the Mach disk position with the corresponding combustion chamber pressure. Notably, a form of hysteresis appears after the maximum pressure is reached. This behavior may be linked to the gradual reduction in nozzle throat diameter caused by the deposition and solidification of alumina on the relatively "cold" nozzle surface, as described in Saile (2021). While the Mach disk location could serve as a useful validation parameter for future numerical simulations, it is not be further analyzed in the present study.

Acknowledgements I would like to express my sincere gratitude to the wind tunnel engineers, in particular Stefan Glumm, for their expertise and dedication in supporting the experimental campaign. Special thanks go to the skilled mechanics from the machine shop for their reliable and precise work in preparing the hardware. I am especially grateful to Viktor Kühl for his valuable engineering support throughout the project, as well as for his help with proofreading, alongside Ciro Salvi and Dr. Thomas Gawehn. I would also like to thank Knut Mannel from LaVision, whose support was instrumental in enabling the PIV measurements. I am further indebted to Daniel Kirchheck and Ciro Salvi for the many fruitful exchanges and discussions that enriched the development and interpretation of this work. Finally, I extend my heartfelt thanks to all those who were involved in and contributed to the success of this project—your support and commitment were essential and deeply appreciated.

Author Contributions Dominik Saile helped in conceptualization, methodology, investigation, data curation, formal analysis, visualization, writing—original draft, writing—review & editing. Viktor Kühl contributed to conceptualization, data acquisition, investigation, review. Ali Gülhan helped in project administration, funding acquisition, supervision, review. All authors have read and approved the final manuscript and agree to be accountable for all aspects of the work.

Funding Open Access funding enabled and organized by Projekt DEAL.

Data Availability No datasets were generated or analyzed during the current study.

Declarations

Conflict of interest The authors declare no conflict of interest.

References

André B, Castelain T, Bailly C (2011) Experimental study of flight effects on screech in underexpanded jets. Phys Fluids 23:126102. https://doi.org/10.1063/1.3671735

Bryce W, Pinker R (1977) The noise from unheated supersonic jets in simulated flight. 4th Aeroacoustics Conference, Atlanta, Georgia, USA, Oct. 3-5, 1977, p.1327

David S, Radulovic S (2005) Prediction of buffet loads on the Ariane 5 afterbody. 6th International Symposium on Launcher Technologies, Munich, Germany

Deck S, Thorigny P (2007) Unsteadiness of an axisymmetric separating-reattaching flow: Numerical investigation. Physics of Fluids 19(6). https://doi.org/10.1063/1.2734996

DFG-TRR40: Technologische Grundlagen für den Entwurf thermisch und mechanisch hochbelasteter Komponenten zukünftiger Raumtransportsysteme. https://www.epc.ed.tum.de/aer/forschung/projekte/sfb/. Accessed: 2025-06-18. 2008 to 2020

Deprés D, Reijasse P, Dussauge JP (2004) Analysis of unsteadiness in afterbody transonic flows. AIAA J 42(12):2541–2550. https://doi.org/10.2514/1.7000

Edgington-Mitchell D, Weightman J, Lock S, Kirby R, Nair V, Soria J, Honnery D (2021) The generation of screech tones by shock leakage. J Fluid Mech 908:A46–1. https://doi.org/10.1017/jfm.2020.945

Edgington-Mitchell D, Li X, Liu N, He F, Wong TY, Mackenzie J, Nogueira P (2022) A unifying theory of jet screech. J Fluid Mech 945 A8. https://doi.org/10.1017/jfm.2022.549

Future European Space Transportation Investigation Programme (FESTIP). https://archives.eui.eu/en/fonds/119158?item=ESA-17227. Accessed: 2025-06-18. 1993

Gentile V, Schrijer FF, Van Oudheusden BW, Scarano F (2016) Afterbody effects on axisymmetric base flows. AIAA J 54(8):2285–2294. https://doi.org/10.2514/1.J054733

Gentile V, Schrijer FFJ, van Oudheusden BW, Scarano F (2016) Very-low frequency wake dynamics of an axisymmetric body. International Workshop on Non-Intrusive Optical Flow Diagnostics, TU Delft Delft, The Netherlands, pp.1–5. https://resolver.tudelft.nl/uuid:c8f768b1-210d-44db-8382-d39b47ad28c0

van Gent PL, Schrijer FF, Van Oudheusden BW (2018) Assessment of the pseudo-tracking approach for the calculation of material acceleration and pressure fields from time-resolved PIV: part I. Error Propag Meas Sci Technol 29(4):045204. https://doi.org/10.1088/1361-6501/aaa0a5

van Gent PL, Payanda Q, Brust SG, van Oudheusden BW, Schrijer FFJ (2019) Effects of exhaust plume and nozzle length on compressible base flows. AIAA J 57(3):1184–1199. https://doi.org/10.2514/1.J057314

Hay JA, Rose EG (1970) In-flight shock cell noise. J Sound Vib 11(4):411–IN3

Kirchheck D, Saile D, Gülhan A (2019) Spectral analysis of rocket wake flow-jet interaction by means of high-speed schlieren imaging. 8th European Conference for Aeronautics and Space Sciences (EUCASS). 1–4 July, Madrid, Spain. https://doi.org/10.13009/EUCASS2019-1057

Kirchheck D, Saile D, Gülhan A (2019) Spectral analysis of generic rocket wake flows with cold and hot exhaust jets. Sonderforschungsbereich/Transregio 40 – Annual Report. https://elib.dlr.de/137429/

Kirchheck D, Saile D, Gülhan A (2021) Rocket wake flow interaction testing in the Hot Plume Testing Facility (HPTF) Cologne. In: Future space-transport-system components under high thermal and mechanical loads. Ed. by Adams NA et al. Springer, Cham, pp.145–162. https://doi.org/10.1007/978-3-030-53847-7_9

Manning T, Lele S (1998) Numerical simulations of shock-vortex interactions in supersonic jet screech. 36th AIAA Aerospace Sciences Meeting and Exhibit, p.282. https://doi.org/10.2514/6.1998-282

Manning T, Lele S (2000) A numerical investigation of sound generation in supersonic jet screech. 6th Aeroacoustics Conference and Exhibit, Lahaina, USA, p.2081 AIAA-2000-2081. https://doi.org/10.2514/6.2000-2081

Pain R, Weiss P-E, Deck S (2014) Zonal detached eddy simulation of the flow around a simplified launcher afterbody. AIAA J 52(9):1967–1979. https://doi.org/10.2514/1.J052743

Pain R, Weiss P-E, Deck S, Robinet, J-C (2019) Large scale dynamics of a high Reynolds number axisymmetric separating/reattaching flow. Physics of Fluids 31(12). https://doi.org/10.1063/1.5121587

Poldervaart LJ, Wijnands APJ, van Moll LHAM, van Voorthuisen EJ (1974) Modes of vibration of two-dimensional jet of air. In: Film produced by University of Technology of Eindhoven, Physic Department - Aerodynamic Group, Netherlands. https://www.youtube.com/watch?v=EnlCDOQW7wc

Poldervaart LJ, Vink AT, Wijnands APJ (1969) Jet screech. In: Film produced for Aerodynamic Division of the Physics Department, G. Vossers, Technological University of Eindhoven. https://www.youtube.com/watch?v=dJp5m1SDN5c

Ponomarenko A (2014) RPA: Tool for rocket propulsion analysis. Space Propulsion Conference, Cologne, Germany

Powell A (1953) On the mechanism of choked jet noise. Proc Phys Soc Sect B 66(12):1039

Powell A (1953) On the noise emanating from a two-dimensional jet above the critical pressure. Aeronaut Q 4(2):103–122

Raman G (1998) Advances in understanding supersonic jet screech: review and perspective. Prog Aerosp Sci 34(1–2):45–106. https://doi.org/10.1016/S0376-0421(98)00002-5

Lê T-H-H (2005) Etude expérimentale du couplage entre l'écoulement transsonique d'arrière-corps et les charges latérales dans les tuyères propulsives. PhD thesis, École Doctorale Sciences pour l'Ingénieur et Aéronautique, France

Saile D (2019) Experimentelle Analyse der Heckströmung von Raumtransportsystemen / Experimental analysis on near-wake flows of space transportation systems. DLR Forschungsbericht, DLR-FB-2019-04 Deutsches Zentrum für Luft- und Raumfahrt / PhD thesis (Dissertation), RWTH Aachen University, Germany

Saile D, Pohl J, Gülhan A (2013) Investigation of hot plume-external flow interaction in the near-wake region of a generic space transportation system geometry in high subsonic flow regime. In: Stemmer C, Adams NA, Haidn OJ, Radespiel R, Sattelmayer T, Schröder W und Weigand B (Editoren), Sonderforschungsbereich/Transregio. 81–93

Saile D, Allofs D, Kühl V, Steffens L, Gülhan A, Beversdorff M, Förster W, Willert C, Carlotti S, Maggi F, Liljedahl M, Wingborg N, Langener T, Eynde Jvd (2021) Characterization of SRM plumes with alumina particulate in subscale testing: fundamental outline and first results of the ESA-EMAP project. CEAS Space J 13:247–268. https://doi.org/10.1007/s12567-020-00338-0

Saile D, Kühl V, Gülhan A (2019) On the subsonic near-wake of a space launcher configuration without jet. Exp Fluids 60(4):50. https://doi.org/10.1007/s00348-019-2690-9

Saile D, Kühl V, Gülhan A (2019) On the subsonic near-wake of a space launcher configuration with exhaust jet. Exp Fluids 60(11):165. https://doi.org/10.1007/s00348-019-2801-7

Saile D, Kühl V, Gülhan A (2021) On subsonic near-wake flows of a space launcher configuration with various base geometries. Exp Fluids 62:122. https://doi.org/10.1007/s00348-021-03149-z

Saile D, Gülhan A (2021) Aeroacoustic coupling effect during the ascent of space transportation systems. AIAA J 59(7):2346–2356. https://doi.org/10.2514/1.J059747

Saile D, Gülhan A, Banuti D, Kitsche W, Henckels A, Wyborny D, Willert Ch, Fischer M, Heinze J, Voges M (2013) Hot plume testing facilities for ELV propulsion characterization. Tech Rep. https://elib.dlr.de/127569/

Schrijer FFJ, Sciacchitano A, Scarano F (2014) Spatio-temporal and modal analysis of unsteady fluctuations in a high-subsonic base flow. Phys Fluids 26(8). https://doi.org/10.1063/1.4891257

Schrijer FFJ, Sciacchitano A, Scarrano F, Hannemann K, Pallegoix J-F, Maseand JEJ, Schwane R (2011) Experimental investigation of base flow buffeting on the Ariane 5 launcher using high speed PIV. 7th European Symposium on Aerothermodynamics 692:103

Stark R, Wagner B (2009) Experimental study of boundary layer separation in truncated ideal contour nozzles. Shock Waves 19(3):185–191. https://doi.org/10.1007/s00193-008-0174-6

Statnikov V, Bolgar I, Scharnowski S, Meinke M, Kähler CJ, Schröder W (2016) Analysis of characteristic wake flow modes on a generic transonic backward-facing step configuration. Eur J Mech -B/Fluids 59:124–134. https://doi.org/10.1016/j.euromechflu.2016.05.008

Statnikov V, Meinke M, Schröder W (2017) Reduced-order analysis of buffet flow of space launchers. J Fluid Mech 815:1–25. https://doi.org/10.1017/jfm.2017.46

Tam CK, Seiner JM, Yu JC (1986) Proposed relationship between broadband shock associated noise and screech tones. J Sound Vib 110(2):309–321. https://doi.org/10.1016/S0022-460X(86)80212-7

Weiss P-E, Deck S, Robinet J-C, Sagaut P (2009) On the dynamics of axisymmetric turbulent separating/reattaching flows. Physics of Fluids 21(7). https://doi.org/10.1063/1.3177352

Weiss PE, Deck S (2013) Numerical investigation of the robustness of an axisymmetric separating/reattaching flow to an external perturbation using ZDES. Flow Turbul Combust 91:697–715. https://doi.org/10.1007/s10494-013-9484-6

Welch P (1967) The use of fast Fourier transform for the estimation of power spectra: a method based on time averaging over short, modified periodograms. IEEE Trans Audio Electroacoust 15(2):70–73

Wolf CC (2014) The subsonic near-wake of bluff bodies. PhD thesis (Dissertation), RWTH Aachen University, Germany